Improved multi-time scale lumped thermoelectric coupling modeling and parameter dispersion evaluation of lithium-ion batteries.
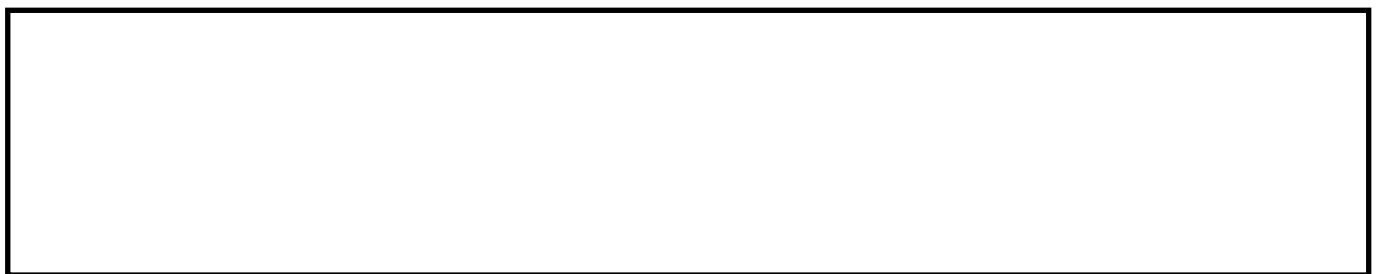
SHI, H., WANG, S., FERNANDEZ, C., YU, C., XU, W., DABLU, B.E. and WANG, L.

2022

Improved multi-time scale lumped thermoelectric coupling modeling and parameter dispersion evaluation of lithium-ion batteries

Haotian Shi[a], Shunli Wang[a*], Carlos Fernandez[b], Chunmei Yu[a], Wenhua Xu[a], Bobobee Etse Dablu[a], Liping Wang[c*]

[a]*School of Information Engineering, Southwest University of Science and Technology, Mianyang 621010, China;*

[b]*School of Pharmacy and Life Sciences, Robert Gordon University, Aberdeen AB10-7GJ, UK;*

[c]*Department of Mechanical Engineering, Tsinghua University, Beijing 100084, China;*

Abstract: The rapid development of new energy fields such as electric vehicles and smart grids has put forward higher requirements for the power management of battery integrated systems. Considering that internal temperature and parameter consistency are important factors affecting battery safety and state estimation accuracy, a lumped thermoelectric coupling model based on the multi-time scale effects of battery dynamics parameter is established in this paper. On this basis, a new multi-feature separation modeling idea is proposed and adopted to complete the development of the strong coupling adaptive asynchronous identification strategy to realize the solution of the model. Specifically, the high-frequency and low-frequency characteristics of the resistor-capacitor link under different time constants are distinguished on different time scales. Three sub-filters based on forgetting factor recursive least squares, extended Kalman filtering and joint Kalman filtering are used to realize the adaptive asynchronous synergistic estimation of battery high-frequency dynamics parameter, low-frequency dynamics parameter and internal temperature. In addition, the filters at different time scales are strongly coupled through the voltage response on the diffusion impedance, and the time scale drive under slow dynamics depends on the current distribution of the test conditions. The experimental results of two long-term cycles show that the proposed strategy exhibits excellent terminal voltage tracking effect and internal temperature estimation accuracy. Finally, the concept of parameter dispersion is proposed and discussed. Compared with the results under the traditional identification method, the proposed strategy reduces the maximum parameter dispersion by 51.9%.

*Corresponding authors at: School of Information Engineering, Southwest University of Science and Technology, Mianyang 621010, China (S. Wang). State Key Laboratory of Tribology and Institute of Manufacturing Engineering, Department of Mechanical Engineering, Tsinghua University, Beijing 100084, China (L. Wang).

E-mail address: *wangshunli@swust.edu.cn* (S. Wang), *lpwang@mail.tsinghua.edu.cn* (L. Wang).

1 Introduction

1.1 Motivation and challenges

As part of the global decarbonization efforts, it is inevitable that batteries as an alternative to petroleum fuels will be increasingly used in clean energy systems such as electric vehicles and smart grids [1]. Among the wide variety of battery types [2-3], lithium-ion batteries have undoubtedly become one of the most popular energy storage tools due to their excellent properties, such as high energy density (> 200 Wh/kg [4]), high cycle life (> 1000 cycles [5]), high operating voltage (> 3.0 V [6]), low-cost performance (< 0.15 USD/Wh [7]), and low power consumption [8]. However, smoke and fires from electric vehicles and other clean energy storage systems have occurred frequently in recent years, mainly due to thermal runaway caused by battery overheating caused by inaccurate internal temperature estimates. This has also become one of the key technologies limiting the development of lithium-ion batteries.

In order to maximize the performance of lithium-ion batteries under the premise of long life and safety, it is necessary to deploy an advanced and reliable battery management system (BMS) in the power supply to monitor various states inside the cell in real time, especially temperature changes [9-10]. In most current researches and applications, the thermal and electrical domains of the battery are modeled separately [11]. Correspondingly, many methods have been developed separately in the field

of thermal and electrical characteristic modeling of batteries [12-13]. An obvious disadvantage of this implementation is that it brings additional computational complexity to the large-scale cascaded battery integration system due to the algorithmic coupling between different system domains. In addition, the mechanism of electrochemical polarization reaction process and concentration polarization reaction process of internal carriers at different time scales has not been paid enough attention in battery modeling. Ignoring the multi-time scale effects of the dynamic characteristic parameters often leads to inaccurate battery modeling performance, which is most obvious in the charge transfer and electric double-layer effects and the diffusion effects of lithium ions in solid particles [14]. To solve the above problems, high-fidelity thermoelectric coupling modeling and efficient parameter identification strategy development are necessary and meaningful in embedded applications of advanced BMS.

1.2 Literature review

For battery cells, changes in temperature have a large impact on the performance of battery modeling. The strong time-varying and environment-dependent thermogenesis makes the internal temperature of cells tend to be higher than the surface temperature. Specifically, related studies have shown that the capacity changes by up to 15% under different ambient temperatures [15-18]. In addition, due to the closed and compact structure, the built-in temperature sensor will bring great safety hazard to the integrated application of the battery. In the early years of modeling research on battery thermal characteristics, representative works include Pals et al. [19] established a zero-dimensional thermal model to model the temperature of lithium polymer batteries as early as 1994. Kim et al. [20] established a one-dimensional heat generation model by solving a first-order partial differential equation, and Torchio et al. [21] developed a two-dimensional battery thermal model based on the finite element volume method. Further, Mei et al. [22] completed the three dimensional temperature field simulation

of the battery using finite element simulation software. However, the above-mentioned zero-dimensional model has the disadvantage of insufficient effective information due to the small amount of calculation, which will lead to low internal temperature estimation accuracy. Although the finite element method can meet the accuracy requirements, it will also cause high computational complexity.

With the development of computer technology, advanced battery thermoelectric coupling modeling methods have been proposed in recent studies. For the changeable environment of electric vehicles or the technical requirements of smart grid energy storage, battery thermoelectric modeling needs to meet at least three conditions at the same time: first, BMS hardware computing complexity requirements; second, adaptability requirements for complex and changeable environments; third, online real-time estimation requirements for internal temperature and terminal voltage. In view of this, electrochemical thermoelectric models [23-29] using a large number of partial differential equations (PDEs) do not seem to meet the requirements of embedded system applications. Under these requirements, the battery thermoelectric coupling modeling strategy developed based on mature circuit theory to achieve effective prediction of internal temperature and terminal voltage has become the most potential solution [30-31]. The main typical studies include and the simplified model of the thermoelectric coupled equivalent circuit developed by Wang et al. in the Ref. [32], where the fitted relationship between the electrical and thermal characteristics parameters is obtained in advance through experiments at different temperatures to provide guidance for the optimal charging strategy of the battery. In addition, Wang et al. [33] developed a fractional-order thermoelectric coupling model, and adopted a particle swarm optimization algorithm to realize the identification of model dynamics and thermodynamics. Furthermore, Chen et al. [34] established a thermoelectric coupled model considering the external short-circuit phenomenon, and Chen et al. [35] used the thermal resistance network model to study the thermal runaway characteristics, which also provided many useful suggestions for the thermoelectric coupling modeling of batteries. As

analyzed in the above literature, the thermoelectric coupling model of the battery should contain a sub-model that fully characterizes the electrical properties and a sub-model that characterizes the thermal properties. A more immediate problem is that high-fidelity battery thermoelectric modelling is highly dependent on a reasonable state estimator and an efficient parameter identification strategy. Therefore, it is equally important to develop an efficient identification strategy and a strongly coupled estimation algorithm considering the internal dynamic characteristics of the battery.

The above thermoelectric coupling modeling studies are basically applicable requirements in terms of internal temperature estimation and terminal voltage prediction accuracy. However, in the thermoelectric coupling modeling and the development of efficient identification strategies, another need to pay attention to is the problem of multi-time scale effects that characterize the internal carrier polarization process parameters [36]. Specifically, in the thermoelectric coupling modeling of the battery, the time constant corresponding to the impedance part of the charge transfer process is significantly different from the time constant of the impedance part of the diffusion process. This difference can reach two orders of magnitude in commercial lithium-ion batteries, the results here are that the charge transfer impedance is achieved on the order of seconds, and the diffusion resistance is achieved on the order of hundred seconds [37] [38]. This is both a challenge and an opportunity for high-fidelity modeling of batteries. Under this phenomenon, the concept of dispersion is proposed in this paper to describe whether the physical meaning of each parameter inside the battery under current excitation is clear or not. Dispersion is opposite to the consistency characteristics of battery parameters, where the correlation is that the greater the dispersion, the worse the consistency of internal parameters. It is worth noting that most of the above modeling strategies focus on the accuracy of internal temperature estimation and terminal voltage prediction, while the dispersion of model parameters is ignored. This inevitably leads to the problem that the physical meaning of the internal parameters of the model is not clear and the

relevant internal states cannot be accurately estimated [39-41]. A typical example is that high-precision ohmic resistance identification results can improve the estimation accuracy of battery state of health [42] [43]. The identification results of model parameters with unclear physical meanings may still achieve a smaller tracking error of terminal voltage, which is one of the main reasons why there are few studies on the dispersion analysis of battery models parameters, especially thermoelectric coupled models.

For the multi-time scale effect problem of parameters, one solution is to increase the order of the model to improve the modeling performance, which inevitably brings about the drawbacks of computational complexity. In detail, in the coexistence of pulsed charging and discharging conditions, the low-frequency diffusion impedance parameters cannot be effectively identified due to the fact that the diffusion impedance link does not have enough valid information. In this problem, Dai et al [45] proposed an adaptive step design idea to achieve model parameter identification by considering the cumulative time duration of the current in the diffusive impedance link, which has a better performance in characterizing the consistency of the low-frequency diffusive impedance parameters. However, the influence of temperature factors, especially internal temperature, on the multi-time scale modelling and identification strategy has not been considered in this paper.

1.3 Idea and contributions

Considering the influence of multi-time scale effect and the internal temperature on battery modeling, this paper proposes a multi-feature separation modeling idea and applies it to the lumped parameter thermoelectric coupling model. The four main contributions of this article are as follows.

(1). A lumped thermoelectric coupling model based on multi-time scale effects is established, in which the battery capacity, open-circuit voltage and entropy thermal coefficient are corrected in real time through accurate internal temperature estimation results.

(2). Based on the two different long-term cycle experiments at three different temperatures, the hysteresis voltage used to correct the open circuit voltage and the heat generation equation is modeled and verified.

(3). A multi-feature separation modelling idea is proposed and based on which a strongly coupled adaptive asynchronous identification strategy is designed to achieve accurate estimation of the battery terminal voltage and internal temperature.

(4). The concept of dispersion is proposed as a percentage of the difference normalized by the identification results, and the rationality and effectiveness of the proposed model are verified by the time constants of different impedance links and the dispersion calculation results of parameters under a series of tests.

1.4 Paper organization

The remainder of this paper is organized as follows: Section **2** introduces the battery thermoelectric coupling model considering multi-time scale effects and the internal temperature correction method. Section **3** proposes the idea of multi-feature separation modeling, based on which the development of strong coupling adaptive asynchronous identification strategy is completed and the overall framework of this strategy is given. Section **4** proposes the concept of parameter dispersion, and gives the experiment and result analysis for terminal voltage tracking effect, internal temperature estimation accuracy and parameter dispersion evaluation. And the conclusions are given in Section **5**.

2 Development of lumped thermoelectric coupling model

2.1 Lumped thermoelectric coupling modeling

Accurate and effective battery equivalent modeling is an important prerequisite for state prediction

and performance optimization. In addition, the equivalent model embedded in the commercial BMS should be relatively simple in structure, but should meet precise requirements in the characterization of electrical and thermal properties. Considering the impact of internal temperature on battery performance and safety, it is necessary to develop a high-accuracy thermoelectric coupling model. The lumped thermoelectric coupling model, consisting of an electrical characteristic sub-model and a thermal characteristic sub-model, is chosen to describe the thermal and electrical dynamics of the battery. As suggested in references [15, 36], the second-order RC model is sufficient to characterize the charge transfer and electric double-layer effects of internal carriers. Therefore, it is reasonable and effective to develop an electronic characteristic electronic model based on a second-order resistance-capacitance (RC) circuit. At the same time, by using the similarity between physical domains, that is, physical systems of the same order have similar dynamic characteristic equations [32], the construction of thermal characteristic sub-models can be effectively realized. Taken together, the structure of the lumped parameter thermoelectric coupling model is shown in Fig. 1 (for brevity, only the name of each element is provided in the figure).
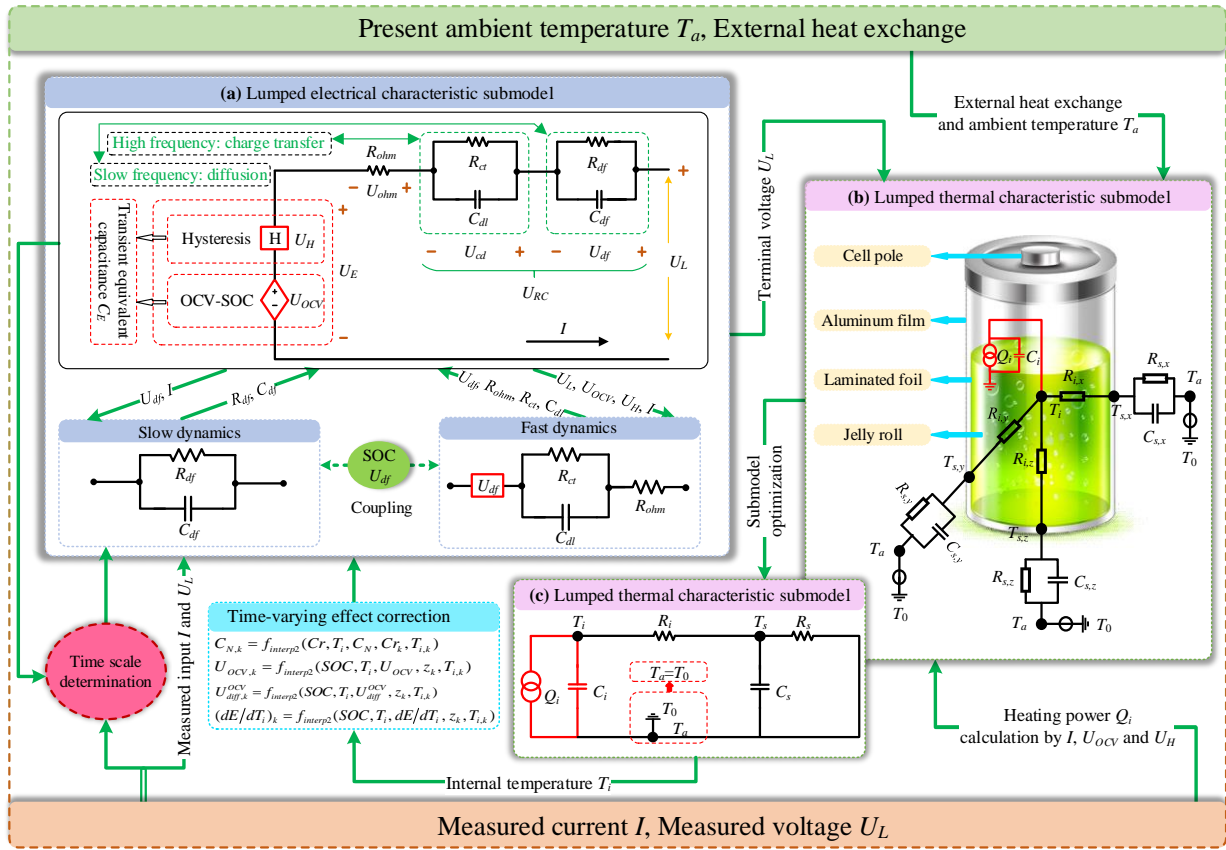
Fig.1. Structural view of lumped thermoelectric coupling model: (a) Electrical characteristic sub-model; (b) Thermal characteristic sub-model; (c) Optimized thermal characteristic sub-model.

As shown in Fig. 1, the lumped thermoelectric coupling model consists of an electrical characteristic sub-model and a thermal characteristic sub-model. In sub- Fig. 1(a), the module H is used to characterize the hysteresis characteristic of the open-circuit voltage (OCV), and the hysteresis voltage at both ends is represented by U_H. It is worth noting that when the sampling time is small enough, the OCV of battery is approximately a capacitor. At this time, C_E can be used to be equivalent to the transient capacitance of the OCV at high-frequency, and U_E is the terminal voltage value of C_E. The impedance characteristics in the electrical characteristics sub-model consist of ohmic resistors and a dual RC circuit network. In the double RC link, the R_{ct}, C_{dl}, R_{df} and C_{df} represent the charge transfer resistance, electric double layer capacitance, diffusion resistance and diffusion capacitance, respectively. Among them, $R_{ct}C_{dl}$ is chosen to characterize the charge transfer and electric double-layer effect phases of carriers, corresponding to the high-frequency dynamic response inside the battery; $R_{df}C_{df}$ is

chosen to characterize the diffusion effect of lithium ions in solid-phase particles, corresponding to the low-frequency dynamic response inside the battery. In addition, the voltages across $R_{ct}C_{dl}$ and $R_{df}C_{df}$ are denoted by U_{cd} and U_{df} respectively, which jointly characterize the multi-time scale effects of battery dynamic parameters.

Sub-Fig. 1(b) is a three-dimensional equivalent model structure for simulating thermal characteristics of the battery. It is worth noting that three-dimensional modeling has high computational complexity, but low modeling complexity is one of the prerequisites for the reliable application and operation of BMS embedded in the later stage. In view of this, the battery thermal characteristics modeling is optimized while ensuring accuracy, and the optimized structure is shown in sub-Fig. 1(c). Among them, Q_i is the total heating power of the battery, which is related to the input current excitation; R_i and R_s represent the internal equivalent thermal resistance and external equivalent thermal resistance, respectively; C_i and C_s represent the internal equivalent thermal capacity and the equivalent thermal capacity of the shell, respectively; T_i, T_s, T_a and T_0 represent the observable internal highest temperature point, surface temperature, ambient temperature and temperature reference point of the battery, respectively. It is worth noting that the ambient temperature T_a is usually set as the temperature reference point T_0, which is more conducive to the integrated application requirements of the battery embedded system. In addition, the simplified scheme of thermal characteristic modeling mentioned above not only meets the requirements of computational complexity, but also considers the material of battery samples. An aluminum case battery sample with excellent thermal conductivity and minimal heat capacity is selected for this study. The internal thermal capacity and thermal resistance parameters of the battery in the three-dimensional direction are basically consistent, thus ensuring the feasibility and effectiveness of the thermal characteristic modeling optimization scheme in sub-Fig. 1(c).

2.2 *Capacity modification and concept of SOC*

Traditionally, the battery state-of-charge (SOC) is usually defined as the percentage of the remaining capacity, which can be found in the Refs. [4, 46]. In the laboratory environment, when the accurate initial SOC value and the nominal capacity of the battery are available, the SOC value calculated by the Coulomb counting method can be used as the reference value of the battery SOC. Its calculation equation is shown in Equation (1).

$$SOC_k = SOC_0 + \Delta t \cdot \sum_{i=1}^{k} I_i / C_N \tag{1}$$

In Equation (1), SOC_0 and SOC_k represent the SOC value of the battery at time 0 and time k respectively; Δt is the sampling time of the BMS; I_i is the input current of the battery; C_N is a fixed value, indicating the nominal battery capacity. It is worth noting that the external environment, such as temperature and Coulombic efficiency, is not fully considered when calculating the true value of SOC. The capacity of the battery changes constantly during operation due to the influence of current rate and temperature. This will cause the calculation error of SOC to adopt the way of nominal capacity [47]. Therefore, it is necessary to pay attention to the impact of the above problems. It is worth mentioning that the data point set of the three-dimensional table obtained by the experiment cannot meet the sampling frequency of the identification algorithm. In other words, in the three-dimensional data table of battery capacity, temperature and current rate, the selection of temperature points and current rate cannot completely correspond to the actual situation. One of the main problems this brings is the need to increase the resolution of the above-mentioned three-dimensional data point set. An effective method is to fit the data set in the three-dimensional table, and the multivariate function obtained in this way can avoid the above problem of inconsistent resolution of data points. In the laboratory situation, a data-based look-up table method with less application but effective is applied in this paper, so as to solve the

problem of inconsistency between the three-dimensional data set and the sampling frequency of the battery system. By considering the time-varying characteristics of battery capacity during operation, the capacity calculation at each moment is given as shown in Equation (2).

$$C_{N,k} = f_{C_N}(Cr_k, T_{i,k}) = f_{interp2}(Cr, T_i, C_N, Cr_k, T_{i,k}) \tag{2}$$

In Equation (2), C_r represents the normalized value of the battery rate; T_i represents the internal temperature of the battery, $C_{n,k}$ is the actual capacity of the battery at time k; $f_{interp2}(*)$ represents the three-dimensional interpolation function. The current rate, temperature and capacity calibration problems can be solved by building a three-dimensional data table. At this time, the linear interpolation function $f_{interp2}(*)$ in Matlab/Simulink is selected, and the actual capacity calculation of the battery at time k is realized by using the current rate acquisition at each moment of operation and the high-precision estimation data of the internal temperature. The specific implementation process of the linear interpolation function $f_{interp2}(*)$ here is to use the value of the known adjacent data points to generate the value of the unknown data point through the difference principle, so that the original data set can be reproduced with a higher resolution data set. Further, the actual capacity at each moment is combined with the idea of the Coulomb counting method, so as to realize the real-time calculation optimization of SOC based on user behavior habits. Based on this, the calculation method of SOC in this paper is given, as shown in Equation (3).

$$z_k = z_{k-1} + \Delta t \cdot I_{k-1}/C_{N,k} \tag{3}$$

In Equation (3), z is the notation representation of the SOC used for brevity, and z_k and z_{k-1} represent the battery SOC values at time k and time k-1 respectively. I_{k-1} is the input current of the battery at time k-1 (defining charging as positive and discharging as negative); $C_{N,k}$ is the actual capacity of the battery at time k. In addition, an important point is that the three-dimensional data table is used to correct the rated capacity value under different charge and discharge rates and temperatures,

so that the SOC estimate value is closer to the current state-of-charge of the battery.

2.3 Model-based modular state representation

2.3.1 Lumped electrical characteristics sub-model

The lumped thermoelectric coupling model consists of two sub-models to describe the electrical

and thermal characteristics of the battery, respectively. For the electrical characteristics sub-model, the

overall terminal voltage consists of the OCV part, the hysteresis voltage part, the voltage of the ohmic

resistance and the voltage part of the dual RC network. Among them, the accurate characterization of

nonlinear OCV is an important part of battery modeling, which has a great impact on the parameter

identification and state prediction of the model. Accurate characterization of nonlinear OCV should also

consider time-varying SOC and temperature effects. Traditionally, the nonlinear OCV of the battery is

modeled by an empirical formula, and its modeling idea has been applied in many Refs. [32, 48-49].

However, we employ a similar approach with multifactorial effects of battery capacity. By establishing

a three-dimensional data table of OCV, SOC and internal temperature, an interpolation function is used

to achieve accurate calculation of battery SOC. This is a more preferable approach in the laboratory

setting, which can effectively reduce the additional computational burden in battery thermoelectric

modeling due to coupled iterations between data. The calculation method of OCV is shown in Equation

(4).

$$U_{OCV,k} = f_{OCV}(z_k, T_{i,k}) = f_{interp2}(SOC, T_i, U_{OCV}, z_k, T_{i,k}) \tag{4}$$

For the hysteresis voltage of the battery, the experimental results show that its value is also affected

by SOC and temperature. It is worth noting that the hysteresis voltage generated by the battery during

each charge-discharge state transition is not a simple linear relationship. Therefore, the input current of

the battery and the transition process of charge and discharge states should be considered in the hysteresis

voltage modeling. First, the error between the charge OCV value and the discharge OCV value at different temperatures is calculated, as shown in Equation (5).

$$U_{diff}^{OCV}(z_k) = \sum_{j=1}^{M}\left(U_{ch,j}^{OCV}(z_k) - U_{dch,j}^{OCV}(z_k)\right)\Big/2M \tag{5}$$

In Equation (5), U_{diff}^{OCV} represents the error between the charging and discharging OCV; $U_{ch,j}^{OCV}$ and $U_{dch,j}^{OCV}$ represent the charging OCV value and discharging OCV value of the j-th group respectively; M represents the number of experimental groups for charging and discharging. The three-dimensional data table of U_{diff}^{OCV}, SOC and temperature can be obtained from the error data between the charging OCV and the discharging OCV at different temperatures, and then the U_{diff}^{OCV} can be accurately obtained in the iterative process of thermoelectric coupling modeling. Further, combined with the step function of the current, the nonlinear iterative calculation of the hysteresis voltage at each moment is realized, as shown in Equation (6).

$$U_{H,k} = f_{U_H}(z_k, T_{i,k}) = \underbrace{\exp\left(-\left|\frac{\Delta t \varepsilon I_{k-1}}{C_{N,k}}\right|\right)}_{A_{H,k-1}} U_{H,k-1} + \underbrace{\left(1 - \exp\left(-\left|\frac{\Delta t \varepsilon I_{k-1}}{C_{N,k}}\right|\right)\right)}_{1-A_{H,k-1}} \operatorname{sgn}(I_{k-1}) U_{diff}^{OCV}(z_{k-1}) \tag{6}$$

In Equation (6), ε is the efficiency factor for the decay rate of the hysteresis voltage; A_H and $1-A_H$ are notation used for simplicity of expression. And then, the port voltage of the dual RC network is used to describe the electrochemical polarization process voltage and concentration polarization process voltage of the battery, which are represented by symbols U_{cd} and U_{df}, respectively. The values of the two can be calculated iteratively through the full response equation of the RC circuit, as shown in Equation (7).

$$U_{cd,k} = \underbrace{\exp\left(-\Delta t/R_{ct,k}C_{dl,k}\right)}_{A_{cd,k}} U_{cd,k-1} + R_{ct,k}\underbrace{\left(1 - \exp\left(-\Delta t/R_{ct,k}C_{dl,k}\right)\right)}_{1-A_{cd,k}} I_{k-1} \tag{7a}$$

$$U_{df,k} = \underbrace{\exp\left(-\Delta t/R_{df,k}C_{df,k}\right)}_{A_{df,k}} U_{df,k-1} + R_{df,k}\underbrace{\left(1 - \exp\left(-\Delta t/R_{df,k}C_{df,k}\right)\right)}_{1-A_{df,k}} I_{k-1} \tag{7b}$$

In Equation (7), A_{cd}, A_{df}, $1-A_{cd}$, and $1-A_{df}$ are symbolic matrix representations used for simplicity of expression. Among them, the time constants of the full response corresponding to A_{cd} and

$1-A_{cd}$ are relatively small, corresponding to the high-frequency characteristics of the internal impedance of the battery; while the time constants of the full response corresponding to A_{df} and $1-A_{df}$ are relatively large, corresponding to the low-frequency characteristics of the internal impedance of the battery. Such different impedance characteristics at different frequencies can provide support for the optimization of thermoelectric coupling modeling. According to the above-mentioned iterative calculation and analysis of the OCV, hysteresis voltage and impedance voltage in the electrical characteristic sub-model, the state-space equation of the lumped electrical characteristic sub-model can be constructed, as shown in Equation (8).

$$\begin{bmatrix} z_{k+1} \\ U_{cd,k+1} \\ U_{df,k+1} \\ U_{H,k+1} \end{bmatrix} = \begin{bmatrix} 1 & 0 & 0 & 0 \\ 0 & A_{cd,k} & 0 & 0 \\ 0 & 0 & A_{df,k} & 0 \\ 0 & 0 & 0 & A_{H,k} \end{bmatrix} \begin{bmatrix} z_k \\ U_{cd,k} \\ U_{df,k} \\ U_{H,k} \end{bmatrix} + \begin{bmatrix} \Delta t/(\eta_I \eta_T \cdot C_{N,0}) & 0 \\ R_{ct,k}(1-A_{cd,k}) & 0 \\ R_{df,k}(1-A_{df,k}) & 0 \\ 0 & \text{sgn}(I_k)(1-A_{H,k}) \end{bmatrix} \begin{bmatrix} I_k \\ U_{diff}^{OCV}(z_k) \end{bmatrix} \tag{8}$$

Assume that the sampling period Δt remains constant during the system input current. Further, based on the above analysis of the terminal voltage of each circuit, the terminal voltage of the lumped electrical characteristic sub-model at time k is calculated as shown in the following Equation (9).

$$U_{L,k} = \underbrace{U_{OCV,k} + U_{H,k}}_{U_{E,k}} - \underbrace{I_k R_{ohm,k}}_{U_{ohm,k}} - \underbrace{(U_{cd,k} + U_{df,k})}_{U_{RC,k}} \tag{9}$$

2.3.2 Lumped thermal characteristics sub-model

For the lumped thermal characteristics sub-model, the conduction process of thermal energy mainly includes two stages: internal heat generation caused by the input current, and heat dissipation to the outside through the electrolyte and the shell. Therefore, the accurate calculation of the heat production inside the battery at all times is the basis of the entire lumped thermoelectric coupling modeling. As suggested by many Refs. [32, 50], the Bernardi equation can be used to calculate the heat production of the battery in operation. However, unlike the direct use of Bernardi's equation in the above literature, the

advantage of lumped thermoelectric coupling modeling is that it allows us to optimize the modeling of battery heat production by considering more constraints. Remember that we optimized the OCV modeling in the electrical properties sub-model in this paper. Based on this, the optimized OCV equation can also be used to calculate the heat production of the battery. The optimized battery heat production calculation is shown in Equation (10).

$$Q_{i,k} = \left(U_{OCV,k} + U_{H,k} - U_{L,k}\right)I_k + I_k T_{i,k} \underbrace{\left(dU_E / dT_i\right)}_{dU_{OCV}/dT_i + dU_H/dT_i} \tag{10}$$

In Equation (10), the differential term dU_E/dT_i, the sum of dU_{OCV}/dT_i and dU_H/dT_i, is the entropy thermal coefficient of the battery, which can be obtained experimentally. It can be seen from Equation (10) that due to the electrical characteristic parameters OCV, hysteresis voltage and battery terminal voltage are considered in the calculation equation of battery heat generation. Therefore, the calculation accuracy of battery heat production is improved due to the consideration of multiple factors. Then, using the modeling similarity between the thermal conduction mode of the battery and the electrical shunt mode, the second-order differential equations of the T_i node and the T_s node in the lumped thermal characteristic sub-model can be easily obtained by combining the circuit laws, as shown in Equation (11) Show.

$$\begin{cases} dT_{ia}/dt = -T_{ia}/R_i C_i + T_{sa}/R_i C_i + Q_i/C_i \\ dT_{sa}/dt = -T_{ia}/R_i C_s + T_{sa}\left(1/R_i C_s + 1/R_s C_s\right) \end{cases} \Leftarrow \begin{cases} T_{ia} = T_i - T_a \\ T_{sa} = T_s - T_a \end{cases} \tag{11}$$

In Equation (11), T_{ia} and T_{sa} represent the difference between the battery temperature and the reference temperature point. Assuming that the sampling period Δt remains unchanged during the system input current, then at time $k+1$, the state equation based on the thermal characteristic sub-model is calculated as shown in Equation (12).

$$\underbrace{\begin{bmatrix} T_{ia,k+1} \\ T_{sa,k+1} \end{bmatrix}}_{x_{d,k+1}} = \underbrace{\begin{bmatrix} 1 - \Delta t/R_iC_i & \Delta t/R_iC_i \\ \Delta t/R_iC_s & 1 - \left(\Delta t/R_iC_s + \Delta t/R_sC_s\right) \end{bmatrix}}_{A_{d,k}} \underbrace{\begin{bmatrix} T_{ia,k} \\ T_{sa,k} \end{bmatrix}}_{x_{d,k}} + \underbrace{\begin{bmatrix} \Delta t/C_i \\ 0 \end{bmatrix}}_{B_{d,k}} \underbrace{[Q_{i,k}]}_{u_k} \tag{12}$$

In Equation (12), x_d is the state matrix in discrete form based on the thermal characteristic sub-model; u_k is the input at time k, representing the heating power; $A_{d,k}$ and $B_{d,k}$ are notational representations for simplicity, representing the system matrix and the control matrix. It is worth noting that from the perspective of embedded system applications, the choice of feedback should be more inclined to measurable physical quantities. Therefore, T_{sa} is selected in the modeling as the output of the thermal properties sub-model. In addition, since the measurement of T_{sa} does not require embedded thermal sensors inside the battery, it is safer for the entire battery embedded system. Based on this, the observation equation of the thermal characteristic sub-model can be obtained, as shown in Equation (13).

$$\underbrace{T_{sa,k+1}}_{y_{d,k}} = \underbrace{\begin{bmatrix} 0 & 1 \end{bmatrix}}_{C_{d,k}} \underbrace{\begin{bmatrix} T_{ia,k} & T_{sa,k} \end{bmatrix}^T}_{x_{d,k}} + \underbrace{[0]}_{D_{d,k}} \underbrace{[Q_{i,k}]}_{u_k} \tag{13}$$

In Equation (12), y_d is the output of the thermal characteristics sub-model in discrete state, representing the surface temperature in the battery; $C_{d,k}$ and $D_{d,k}$ are notational representations for simplicity, representing the output matrix and direct transfer matrix of the thermal characteristic sub-model observation equation at time k. It should be noted that in the observation equation of the thermal characteristic sub-model, there is no direct coupling relationship between the output and the input, so $D_{d,k}$ is equal to 0 in this study.

3 LTECM-based multi-feature separation modeling mechanism

3.1 Multi-feature separation modeling architecture

As mentioned above, the inherent impedance characteristics of the battery are manifested in different frequency bands, which are caused by the internal carrier transport mechanism, that is, the

multi-time scale effect of the internal parameters. In order to make better use of this characteristic to optimize the lumped thermoelectric coupling modeling, we use a separate dual RC circuit modeling to characterize the impedance characteristics of the polarization response at different frequency bands. Correspondingly, the $R_{ct}C_{dl}$ part corresponds to the high-frequency characteristics of the electrochemical polarization process, and the time constant is small, while the $R_{df}C_{df}$ part corresponds to the low-frequency characteristics of the concentration polarization process, and the time constant is large. In addition, the internal temperature of the battery should be accurately known at all times in the application. In other words, the internal temperature of the battery needs to be accurately estimated in both high and low-frequency bands. In view of this, we propose a strongly coupled adaptive asynchronous identification strategy (SCAAIS) to solve the multi-time scale problem of model parameters. The difference from the traditional method is that SCAAIS utilizes a novel multi-feature separation modeling idea to distinguish the electro-thermal parameters under different dynamic reaction time constants and identify them on different time scales. The principle of the multi-feature separation modeling idea under the lumped parameter thermoelectric coupling model is shown in Fig.2.
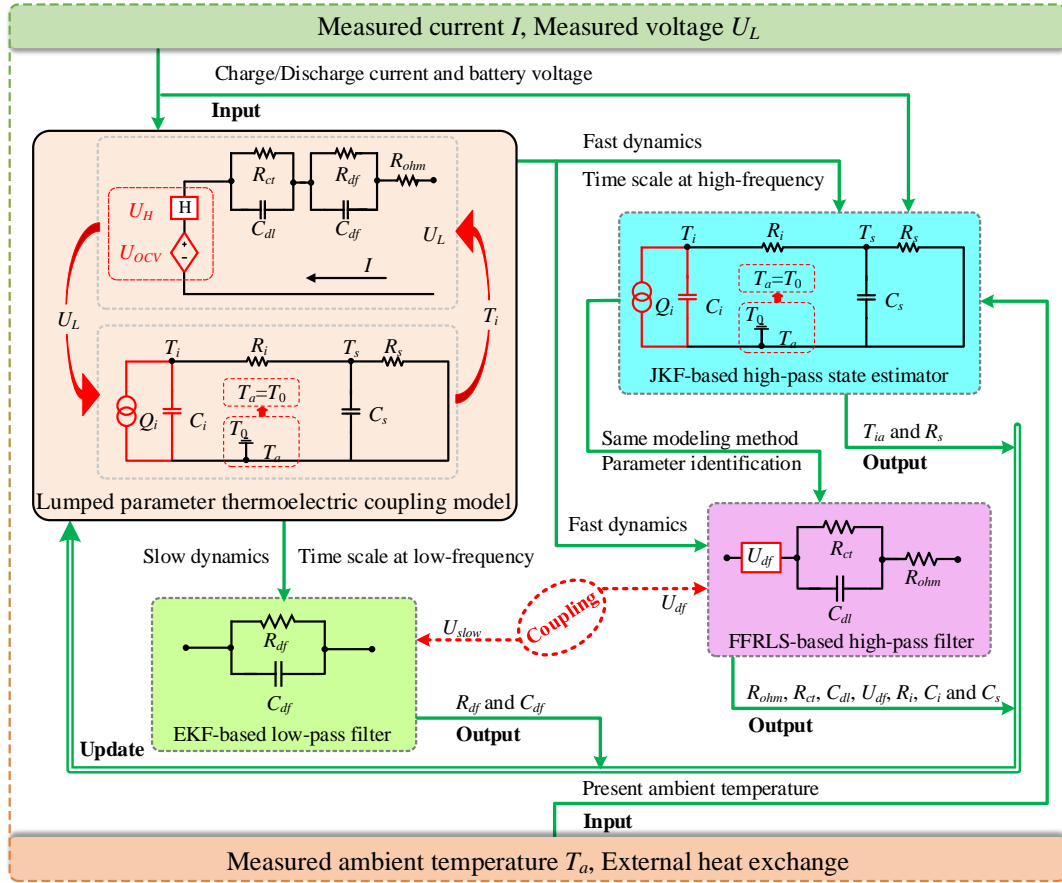
Fig. 2. Architecture of multi-feature separation modeling idea

As shown in Fig. 2, the idea of multi-feature separation modeling naturally divides the parameters

in the lumped thermoelectric coupling model into fast dynamics and slow dynamics, which correspond

to the high-frequency and low-frequency characteristics of the parameters respectively. The parameters

that need to be identified under fast dynamics include ohmic resistance, charge transfer and electric

double-layer impedance, and the internal temperature estimation part of the thermal characteristics sub-

model. The parameter to be identified under slow dynamics is the diffusion resistance of ions in solid

particles. The realization of the strong coupled adaptive asynchronous identification strategy based on

the multi-feature separation modeling idea is completed by three separate filters. Among them, the sub-

algorithm module under high-frequency dynamics consists of two high-pass filters. The sub-algorithm

module under the low-frequency dynamics consists of a specially designed low-pass filter. In addition,

Fig. 2 also describes the coupling mechanism between the multi-time-scale electrical characteristic sub-

model and the thermal characteristic sub-model. It is to feed back the terminal voltage prediction results obtained under the identification strategy of the electrical characteristic sub-model to the thermal characteristic sub-model in real time, so as to realize the accurate calculation of the battery heat production and further complete the accurate prediction of the internal temperature.

3.2 Model-based sub-algorithm design for parameter identification

3.2.1 Sub-algorithm development under fast dynamics

The lumped thermoelectric coupling model based on the idea of multi-feature separation modeling can improve the consistency performance of battery internal parameters. However, the multi-physics coupling in the model also puts forward certain technical innovation requirements for algorithm development. Nonetheless, if we look at it from a different angle, its multi-feature separation modeling points the way for the development of model sub-algorithms. In this problem, we first need to clarify the different parameter sets to be identified under fast dynamics and slow dynamics. The parameter sets to be identified for fast dynamics mainly include: R_{ohm}, R_{ct}, U_{dl}, R_i, C_i, R_s and C_s. Therefore, under this idea of multi-feature separation modeling considering multiple time scales, we first define:

$$U_{p,k} = U_{L,k} - U_{OCV,k} - U_{H,k} = I_k R_{ohm,k} + U_{cd,k} + U_{df,k} \tag{14}$$

In Equation (14), the values of U_{OCV} and U_H after SOC and internal temperature correction can be directly determined by looking up the table through experiments. Then, according to the state-space equation of the electrical characteristic sub-model and the thermal characteristic sub-model, we can obtain the frequency domain form of the fast dynamics in the lumped thermoelectric coupling model, as shown in Equation (15).

$$G_{ele}(s) = U_p(s)/I(s) = -R_{ohm} - R_{ct}/(1 + R_{ct}C_{dl}s) - U_{df}(s) \tag{15a}$$

$$G_{the}(s) = T_{ia}(s)/Q_i(s) = \left(R_sC_sR_is + R_i + R_s\right)/\left(R_sC_sC_is^2 + \left(R_sC_s + R_sC_i + R_iC_i\right)s + 1\right) \quad (15b)$$

In Equation (15), the Equation (15a) represents the transfer function of the fast dynamics in the electronic characteristic sub-model, represented by the function $G_{ele}(s)$; the Equation (15b) represents the transfer function of the fast dynamics in the thermal characteristic sub-model, represented by the function $G_{the}(s)$. Further, the difference equation form of the electrical characteristic sub-model and the thermal characteristic sub-model can be obtained, as shown in Equation (16).

$$U_{p,k} = \alpha_1 U_{p,k-1} + \alpha_2 I_k + \alpha_3 I_{k-1} + \alpha_4 \quad (16a)$$

$$T_{ia,k} = \beta_1 T_{ia,k-1} + \beta_2 T_{ia,k-2} + \beta_3 Q_{i,k-1} + \beta_4 Q_{i,k-2} \quad (16b)$$

In Equation (16), the Equation (16a) is the difference equation of the electrical characteristic sub-model, where α_1, α_2, α_3 and α_4 are the coefficients to be identified; the Equation (16b) is the difference equation of the lumped thermal characteristic sub-model, where $\beta_1, \beta_2, \beta_3$ and β_4 are the coefficients to be identified. The specific expanded form of these parameters to be identified is shown in Equation (17).

$$\alpha_1 = R_{ct}C_{dl}/\left(\Delta t + R_{ct}C_{dl}\right) \quad (17a)$$

$$\alpha_2 = \left(\left(R_{ohm} + R_{ct}\right)\Delta t + R_{ohm}R_{ct}C_{dl}\right)/\left(\Delta t + R_{ct}C_{dl}\right) \quad (17b)$$

$$\alpha_3 = R_{ohm}R_{ct}C_{dl}/\left(\Delta t + R_{ct}C_{dl}\right) \quad (17c)$$

$$\alpha_4 = \left(\left(\Delta t + R_{ct}C_{dl}\right)U_{df,k} - R_{ct}C_{dl}U_{df,k-1}\right)/\left(\Delta t + R_{ct}C_{dl}\right) \quad (17d)$$

$$\beta_1 = -\Delta t/R_iC_i - \Delta t/R_sC_s - \Delta t/R_iC_s + 2 \quad (17e)$$

$$\beta_2 = (1 - \Delta t/R_iC_i)(\Delta t/R_sC_s + \Delta t/R_iC_s - 1) \quad (17f)$$

$$\beta_3 = \Delta t/C_i \quad (17g)$$

$$\beta_4 = (\Delta t/C_i)(\Delta t/R_sC_s + \Delta t/R_iC_s - 1) \quad (17h)$$

Then, we can simply describe the problem as how to identify the coefficient matrix online with known sampled data. Considering that the forgetting factor recursive least squares (FFRLS) method is

widely used in system identification, the feasibility and effectiveness of the method have been demonstrated in many applications [32, 41, 48, 51]. Therefore, the FFRLS method is applied in this paper to realize the online identification of the electrical and thermal parameters under the fast dynamics in the lumped thermoelectric coupling model. In view of this, we define an exogenous autoregressive model for the online iterative identification method, as shown in Equation (18).

$$\underbrace{\begin{bmatrix} Y_{ele,k} \\ Y_{the,k} \end{bmatrix}}_{Y_{fast,k}} = \underbrace{\begin{bmatrix} \boldsymbol{\theta}_{ele,k} \\ \boldsymbol{\theta}_{the,k} \end{bmatrix}}_{\boldsymbol{\theta}_{fast,k}} \underbrace{\begin{bmatrix} H_{ele,k} \\ H_{the,k} \end{bmatrix}^{T}}_{H_{fast,k}} \tag{18}$$

In Equation (18), $Y_{fast,k}$ is the data output matrix of fast dynamics at time k. $\boldsymbol{\theta}_{fast,k}$ is the coefficient matrix to be identified at time k. $H_{fast,k}$ is the data input matrix of fast dynamics at time k. The definitions of the above matrices are as follows:

$$H_{fast,k} = \begin{bmatrix} H_{ele,k} \\ H_{the,k} \end{bmatrix} = \begin{bmatrix} U_{P,k-1} & I_{k} & I_{k-1} & 1 \\ T_{ia,k-1} & T_{ia,k-2} & Q_{i,k-1} & Q_{i,k-2} \end{bmatrix} \tag{19a}$$

$$\boldsymbol{\theta}_{fast,k} = \begin{bmatrix} \boldsymbol{\theta}_{ele,k} \\ \boldsymbol{\theta}_{the,k} \end{bmatrix} = \begin{bmatrix} \alpha_{1,k} & \alpha_{2,k} & \alpha_{3,k} & \alpha_{4,k} \\ \beta_{1,k} & \beta_{1,k} & \beta_{1,k} & \beta_{1,k} \end{bmatrix} \tag{19b}$$

$$Y_{fast,k} = \begin{bmatrix} Y_{ele,k} & Y_{the,k} \end{bmatrix}^{T} = \begin{bmatrix} U_{p,k} & T_{ia,k} \end{bmatrix}^{T} \tag{19c}$$

According to the above discussion, we can obtain the FFRLS full sequence loop recursion iteration based on known sampled data as shown below.

At the time $k = 0$, Initialization:

Initialize the coefficient matrix and error covariance matrix following:

$$\hat{\boldsymbol{\theta}}_{fast,0} = E[\boldsymbol{\theta}_{fast,0}] \tag{20a}$$

$$\boldsymbol{P}_{fast,0} = [(\hat{\boldsymbol{\theta}}_{fast,0} - \boldsymbol{\theta}_{fast,0})(\hat{\boldsymbol{\theta}}_{fast,0} - \boldsymbol{\theta}_{fast,0})^{T}] \tag{20b}$$

At the time $k = 1, 2, ...$, repeat:

1. Calculate the gain matrix $K^{\theta}_{fast,k}$ using:

$$K_{fast,k}^{\theta} = \left(\boldsymbol{P}_{fast,k-1}\boldsymbol{H}_{fast,k}\right)\Big/\left(\lambda + \boldsymbol{H}_{fast,k}^{T}\boldsymbol{P}_{fast,k-1}\boldsymbol{H}_{fast,k}\right) \tag{21}$$

2. Update the correlation matrix $\boldsymbol{P}_{fast,k}$ and the coefficient matrix $\widehat{\boldsymbol{\theta}}_{fast,k}$ using:

$$\boldsymbol{P}_{fast,k} = \boldsymbol{P}_{fast,k-1} - K_{fast,k}^{\theta}\boldsymbol{H}_{fast,k}^{T}\boldsymbol{P}_{fast,k-1}\Big/\lambda \tag{22a}$$

$$\hat{\boldsymbol{\theta}}_{fast,k} = \hat{\boldsymbol{\theta}}_{fast,k-1} + K_{fast,k}^{\theta}\left(\boldsymbol{Y}_{fast,k} - \hat{\boldsymbol{\theta}}_{fast,k-1}\boldsymbol{H}_{fast,k}^{T}\right) \tag{22b}$$

After iteratively obtaining $\alpha_1, \alpha_2, \alpha_3, \alpha_4, \beta_1, \beta_2, \beta_3$ and β_4 with FFRLS，we can calculate the

electrical characteristic parameters under fast kinetics using Equations (17a)-(17c), and the thermal

characteristic parameters using Equations (17e)-(17h). On the basis of the identification results of the

electrical characteristic parameters, the diffusion voltage U_{df} response for each sampling period can

be calculated using Equation (17d). Furthermore, in the iterations of the method in this study, we set the

value of the forgetting factor λ equal to 0.98.

3.2.2 Sub-algorithm development under slow dynamics

In traditional battery modeling, the parameter identification is completed in the same time scale,

and the reaction mechanism reflecting internal electrochemical polarization and concentration

polarization cannot be distinguished. For this problem, we consider the difference of the response

frequency of the charge transfer process, the electric double layer process and the diffusion process in

the thermoelectric coupling modeling, and then realize the parameters identification at different

frequencies inside the battery in the form of multi-feature separation modeling. At this time, an important

issue is the development of parameters identification sub-algorithm for slow dynamics. To realize

collaborative identification of model parameters at different time scales, a natural solution is to fix two

different sampling periods after human intervention in low-pass and high-pass filters, respectively [14,

44]. An obvious disadvantage caused by this is that the algorithm cannot adaptively match the current

conditions. In this paper, we use a more intelligent approach to sub-algorithm development under slow

dynamics, and the specific scheme is as follows.

The reaction time of concentration polarization shows that the reaction time constant of $R_{df}C_{df}$ network is much larger than that of $R_{ct}C_{dl}$ network under the same system current excitation. This indicates the fact that the $R_{df}C_{df}$ link itself can be used alone as a low-pass filter for algorithm development. Under this idea, we take the port voltage U_{df} of the diffusion impedance $R_{df}C_{df}$ as the input information. It is worth noting that the amount of change in U_{df} is directly related to the accumulation time of the current excitation on the $R_{df}C_{df}$ network, and the same current excitation through the $R_{df}C_{df}$ network also passes through the OCV module in the lumped parameter thermoelectric coupling model. The result of this process is that the change of U_{df} is indirectly related to the change of SOC. Therefore, we can realize the conditional constraint setting of the sub-algorithm in the low-pass filter through the variation of SOC. In addition, it should be noted that a small SOC change will bring a small U_{df} change, and a too small U_{df} change will easily cause the system to generate an ill-conditioned matrix during the iterative calculation of the algorithm. Therefore, in order to enable the algorithm to adapt to any current condition, and to allow the sub-algorithm under slow dynamics to collect enough valuable information in each run, we set the starting conditions for the low-pass filter as follows:

$$\Delta z \geq 0.5\% \Longleftarrow \Delta z = \Delta t \cdot \sum_{j=0}^{m} I_j \Big/ \eta_l \eta_T C_{N,0} \qquad (23)$$

In Equation (23), m is a multiple of the sampling period Δt of the system. The equation shows that after m sampling periods, the change in SOC is Δz. Every time Δz reaches the condition of greater than or equal to 0.5%, I_j will start counting again from I_0 until the next Δz is greater than or equal to 0.5%. It is worth noting that the selection of Δz as 0.5% is an empirical basis based on the OCV-SOC curve. Observing the flat period of the OCV-SOC curve of the battery sample (commercial

LiFePO4 battery model HTCNR18650) selected by this research, it is found that when the change of SOC is 0.5%, the corresponding OCV value is about 80 mV to 120 mV. The voltage value changes are sufficient for efficient iteration of the algorithm. In addition, the design of the above adaptive step size has at least two obvious benefits. They are: first, compared with the design of fixed high-frequency step size, the data saturation phenomenon of fast dynamic parameters is avoided; second, compared to the design with fixed low-frequency step size, the information loss phenomenon of fast dynamic parameters is avoided.

Because there are fewer effective innovations observable in the low-pass filter under slow dynamics. Therefore, the extended Kalman filtering (EKF) method is chosen to design the sub-algorithm in the low-pass filter. Furthermore, the feasibility and effectiveness of the EKF method for system identification has been demonstrated in many references [3, 8, 27, 52, 53]. Based on this, we first define the parameter matrix to be identified at low-frequency as the state variable of the low-pass filter, namely $\boldsymbol{\rho}_{slow,k} = [R_{df,k} \quad C_{df,k}]$. Then, using the full response expression of the $R_{df}C_{df}$ network, we can obtain the state-space equation under slow response, as shown in Equation (24).

$$\boldsymbol{\rho}_{slow,k+1} = \boldsymbol{\rho}_{slow,k} + \boldsymbol{w}_k \tag{24a}$$

$$U_{slow,k+1} = \exp\left(\frac{-\Delta t}{R_{2,k}C_{2,k}}\right)U_{slow,k} + R_{2,k}\left(1-\exp\left(\frac{-\Delta t}{R_{2,k}C_{2,k}}\right)\right)I_k + v_k \tag{24b}$$

In Equation (24), the Equation (24a) illustrates the slowly changing process of the low-frequency parameter $R_{df}C_{df}$, which is modeled by the noise w_k; the Equation (24b) is the observed value of the voltage across the cell diffusion impedance $R_{df}C_{df}$, denoted by $U_{slow,k+1}$, and its observation error is modeled by the noise v_k. Assuming that the above noises are all independent Gaussian white noises with zero mean and covariance Q_w and R_v. In this papper, the specific information for the establishment of the initial values of w_k and v_k is: $w_k \sim N(0, Q_w)$, $v_k \sim N(0, R_v)$, $Q_w = 10^{-8} \times$

$diag[2.0, 1.0]$, R_v=0.00001. And then, the covariance matrix of w_k and v_k can be expressed by the following Equation (25).

$$P_w = E(w \times w^T), P_v = E(v \times v^T) \tag{25}$$

It is worth noting that the identification accuracy of $R_{df}C_{df}$ cannot be guaranteed only by Equation (24a). Similarly, the accuracy of the $R_{df}C_{df}$ port voltage obtained by iterative Equation (24b) cannot be fully guaranteed. In other words, the inaccurate identification of the low-frequency parameters R_{df} and C_{df} will also cause the diffusion voltage calculation of Equation (24b) to deviate from the true value. Note that the diffusion voltage U_{df} can also be calculated for each sampling period using Equation (17d) under fast kinetics. In addition, since U_{df} is the identification result after the convergence of the fast dynamics sub-algorithm, this value can be considered to have high confidence. Therefore, we can use the U_{df} identified under the fast dynamics as the true value, and compare it with the diffusion voltage iteration value U_{slow} based on Equation (24b). This enables the parameter identification system under slow dynamics to form an effective feedback correction mechanism. Under this feedback mechanism, we develop an EKF-based sub-algorithm for low-frequency filters in slow dynamics. Based on this idea, first define the function as shown in Equation (26).

$$h(U_{slow,k}, I_k, \boldsymbol{\rho}_{slow,k}) = \exp\left(\frac{-\Delta t}{R_{2,k}C_{2,k}}\right) U_{slow,k} + R_{2,k}\left(1 - \exp\left(\frac{-\Delta t}{R_{2,k}C_{2,k}}\right)\right) I_k \tag{26}$$

Then, under the definition of Equation (26), the output matrix $C_{slow,k}^{\boldsymbol{\rho}}$ required by the EKF algorithm is solved, and its calculation is shown in Equation (27).

$$C_{slow,k}^{\boldsymbol{\rho}} = \left. \frac{\partial h(U_{slow,k}, I_k, \boldsymbol{\rho}_{slow,k})}{\partial \boldsymbol{\rho}_{slow}} \right|_{\boldsymbol{\rho}_{slow} = \hat{\boldsymbol{\rho}}_{slow,k}^-} \tag{27a}$$

$$\frac{\partial h(U_{slow,k}, I_k, \boldsymbol{\rho}_{slow,k})}{\partial \boldsymbol{\rho}_{slow}} = \frac{\partial h(U_{slow,k}, I_k, \boldsymbol{\rho}_{slow,k},)}{\partial \boldsymbol{\rho}_{slow}} + \frac{\partial h(U_{slow,k}, I_k, \boldsymbol{\rho}_{slow,k})}{\partial U_{slow,k}} \frac{dU_{slow,k}}{d\boldsymbol{\rho}_{slow}} \tag{27b}$$

In the above Equation (27), the detailed calculation process of each part in the output matrix $C_{slow,k}^{\boldsymbol{\rho}}$

is shown in Equation (28):

$$\frac{\partial h\left(U_{slow,k},I_k,\boldsymbol{\rho}_{slow,k}\right)}{\partial \boldsymbol{\rho}_{slow}} = \left[\frac{\partial h\left(U_{slow,k},I_k,\boldsymbol{\rho}_{slow,k}\right)}{\partial R_{df}} \quad \frac{\partial h\left(U_{slow,k},I_k,\boldsymbol{\rho}_{slow,k}\right)}{\partial C_{df}} \right] \tag{28a}$$

$$\frac{\partial h\left(U_{slow,k},I_k,\boldsymbol{\rho}_{slow,k}\right)}{\partial R_{df}} = \frac{U_{slow,k}\Delta t - R_{df,k}I_k\Delta t}{\left(R_{df,k}\right)^2 C_{df,k}} \exp\left(\frac{-\Delta t}{R_{df,k}C_{df,k}}\right) + I_{k-1}\left(1-\exp\left(\frac{-\Delta t}{R_{df,k}C_{df,k}}\right)\right) \tag{28b}$$

$$\frac{\partial h\left(U_{slow,k},I_k,\boldsymbol{\rho}_{slow,k}\right)}{\partial C_{df}} = \frac{U_{slow,k}\Delta t - R_{df,k}I_k\Delta t}{R_{df,k}\left(C_{df,k}\right)^2} \exp\left(\frac{-\Delta t}{R_{df,k}C_{df,k}}\right) \tag{28c}$$

$$\frac{\partial h\left(U_{slow,k},I_k,\boldsymbol{\rho}_{slow}\right)}{\partial U_{slow,k}} = \exp\left(\frac{-\Delta t}{R_{df,k}C_{df,k}}\right) \tag{28d}$$

$$\frac{dU_{slow,k}}{d\boldsymbol{\rho}_{slow}} = \frac{\partial h\left(U_{slow,k-1},I_{k-1},\boldsymbol{\rho}_{slow}\right)}{\partial \boldsymbol{\rho}_{slow}} + \frac{\partial h\left(U_{slow,k-1},I_{k-1},\boldsymbol{\rho}_{slow}\right)}{\partial U_{slow,k-1}}\frac{dU_{slow,k-1}}{d\boldsymbol{\rho}_{slow}} \tag{28e}$$

$$\frac{\partial h\left(U_{slow,k-1},I_{k-1},\boldsymbol{\rho}_{slow,k-1}\right)}{\partial \boldsymbol{\rho}_{slow}} = \left[\frac{\partial h\left(U_{slow,k-1},I_{k-1},\boldsymbol{\rho}_{slow,k-1}\right)}{\partial R_{df}} \quad \frac{\partial h\left(U_{slow,k-1},I_{k-1},\boldsymbol{\rho}_{slow,k-1}\right)}{\partial C_{df}} \right] \tag{28f}$$

$$\frac{\partial h\left(U_{slow,k-1},I_{k-1},\boldsymbol{\rho}_{slow,k-1}\right)}{\partial R_{df}} = \frac{U_{slow,k-1}\Delta t - R_{df,k-1}I_{k-1}\Delta t}{\left(R_{df,k-1}\right)^2 C_{df,k-1}} \exp\left(\frac{-\Delta t}{R_{df,k-1}C_{df,k-1}}\right) + I_{k-1}\left(1-\exp\left(\frac{-\Delta t}{R_{df,k-1}C_{df,k-1}}\right)\right) \tag{28g}$$

$$\frac{\partial h\left(U_{slow,k-1},I_{k-1},\boldsymbol{\rho}_{slow,k-1}\right)}{\partial C_{df}} = \frac{U_{slow,k-1}\Delta t - R_{df,k-1}I_{k-1}\Delta t}{R_{df,k-1}\left(C_{df,k-1}\right)^2} \exp\left(\frac{-\Delta t}{R_{df,k-1}C_{df,k-1}}\right) \tag{28h}$$

$$\frac{\partial h\left(U_{slow,k-1},I_{k-1},\boldsymbol{\rho}_{slow,k-1}\right)}{\partial U_{slow,k-1}} = \exp\left(\frac{-\Delta t}{R_{df,k-1}C_{df,k-1}}\right) \tag{28i}$$

From Equation (28e), it can be found that there is a recursive mechanism in the above derivation. Under this recursive logic, the calculation of $dU_{slow,k}/d\boldsymbol{\rho}_{slow}$ can be implemented iteratively by initializing $\boldsymbol{\rho}_{slow,k}$ and $dU_{slow,0}/d\boldsymbol{\rho}_{slow}$, and finally the output matrix $C_{slow,k}^{\boldsymbol{\rho}}$ is obtained. Then, the identification of R_{df} and C_{df} is achieved using the EKF sub-algorithm in the low-frequency filter on a separate time scale. The main iterative equations of the sub-algorithm based on EKF are as follows：

At the time $k=0$, Initialization:

Initialize the correlation matrix of the sub-algorithm in the low-pass filter:

$$\hat{\boldsymbol{\rho}}_{slow,0}^+ = E(\boldsymbol{\rho}_{slow,0}) \tag{29a}$$

$$dU_{slow,0}/d\boldsymbol{\rho}_{slow} = \begin{bmatrix} 0 & 0 \end{bmatrix} \tag{29b}$$

$$\boldsymbol{P}_{slow,0}^+ = E[(\boldsymbol{\rho}_{slow,0} - \hat{\boldsymbol{\rho}}_{slow,0}^+)(\boldsymbol{\rho}_{slow,0} - \hat{\boldsymbol{\rho}}_{slow,0}^+)^T] \tag{29c}$$

At the time $k = 1,2, ...,$ repeat:

1. One-step prediction of electrical characteristic parameters in slow dynamics using:

$$\hat{\boldsymbol{\rho}}_{slow,k}^- = \hat{\boldsymbol{\rho}}_{slow,k-1}^+ \tag{30a}$$

$$\boldsymbol{P}_{slow,k}^- = \boldsymbol{P}_{slow,k-1}^+ + \boldsymbol{P}_w \tag{30b}$$

2. One-step correction of electrical characteristic parameters in slow dynamics using:

$$K_{slow,k}^{\rho} = \boldsymbol{P}_{slow,k}^- \left(\boldsymbol{C}_{slow,k}^{\rho}\right)^T \left(\boldsymbol{C}_{slow,k}^{\rho} \boldsymbol{P}_{slow,k}^- (\boldsymbol{C}_{slow,k}^{\rho})^T + P_v\right)^{-1} \tag{31a}$$

$$\hat{\boldsymbol{\rho}}_{slow,k}^+ = \hat{\boldsymbol{\rho}}_{slow,k}^- + K_{slow,k}^{\rho}\left(U_{df,k} - h\left(U_{slow,k}, I_k, \hat{\boldsymbol{\rho}}_{slow,k}^-\right)\right) \tag{31b}$$

$$\boldsymbol{P}_{slow,k}^+ = \left(\boldsymbol{E} - K_{slow,k}^{\rho}\boldsymbol{C}_{slow,k}^{\rho}\right)\boldsymbol{P}_{slow,k}^- \tag{31c}$$

In Equations (29) to (31), $\hat{\boldsymbol{\rho}}_{slow,k}^-$ and $\hat{\boldsymbol{\rho}}_{slow,k}^+$ are the prior and posterior estimates of the slow dynamics parameters at time k, respectively; $\boldsymbol{P}_{slow,k}^-$ and $\boldsymbol{P}_{slow,k}^+$ are the prior and posterior estimates of the error covariance matrix at time k; $K_{slow,k}^{\boldsymbol{\rho}}$ is the Kalman gain matrix of the EKF sub-algorithm in the low-frequency filter at time k; $\boldsymbol{E}$ represents the identity matrix. It is worth noting that at time $k=0$, we initialize $dU_{slow,0}/d\boldsymbol{\rho}_{slow}$ to a zero matrix, and as the iteration proceeds, the value of $dU_{slow,k}/d\boldsymbol{\rho}_{slow}$ will tend to be accurate. In addition, at time k, the identification result of $U_{df,k}$ under the fast dynamics is used as the real value of the voltage of the $R_{df}C_{df}$ network, and it is compared with the voltage observation value $U_{slow,k}$ at both ends of R_{df} and C_{df}. In the iterative process of the algorithm, the one-step prediction result of the low-frequency parameters is modified under the action of the Kalman gain matrix $K_{slow,k}^{\boldsymbol{\rho}}$. Thus, accurate identification of R_{df} and C_{df} is achieved on separate time scales.

3.2.3 Co-estimation of the R_s and internal temperature

Based on the previous elaboration, Equations (17e) to (17h) are used to calculate the thermal characteristic parameters in the lumped thermocouple and the model. It is worth noting that two factors, the material of the battery and the external thermal regulation method, need to be considered in the characterization of the internal thermal behavior. It has been proved by relevant Refs [32, 51] that the values of internal thermal resistance R_i, internal thermal capacity C_i and shell thermal capacity C_s are only related to the material of the battery and remain basically unchanged under different current excitations of the system. However, the value of the external thermal resistance R_s varies with different heat transfer coefficients. The change of heat transfer coefficient can be produced by different system thermal regulation methods and experimental environment. Therefore, the uncertainty of R_s cannot be ignored in lumped thermoelectric coupling modeling. To solve this problem, we develop an adaptive co-estimator algorithm based on joint Kalman, which couples the online adaptive identification of R_s and the estimation of the internal temperature. Under this idea, combining Equations (12) to (13), the state-space equation suitable for the co-estimation of R_s and internal temperature can be obtained, as shown in Equation (32).

$$R_{s,k+1} = R_{s,k} + r_k^1 \tag{32a}$$

$$\boldsymbol{x}_{d,k+1} = \boldsymbol{A}_{d,k}\boldsymbol{x}_{d,k} + \boldsymbol{B}_{d,k}u_k + r_k^2 \tag{32b}$$

$$y_{d,k} = \boldsymbol{C}_{d,k}\boldsymbol{x}_{d,k} + \boldsymbol{D}_{d,k}u_k + e_k \tag{32c}$$

In Equation (32), r_k^1 and r_k^2 are the process noise at time k; e_k is the observation noise at time k. Furthermore, the Equation (32a) shows the variation process of the external equivalent thermal resistance R_s, which is modeled by the noise r_k^1. Suppose we define the state variable matrix of the lumped thermal behavior sub-model as $x_{J,k} = [R_{s,k}, T_{ia,k}, T_{sa,k}]^T$. Then, the state-space equation of the

sub-algorithm for the co-estimation of adaptive R_s and internal temperature can be constructed according to Equations (32a) to (32c), as shown in Equation (33).

$$x_{J,k+1} = f(x_{J,k}, u_{J,k}) + r_k \approx A_{J,k}x_{J,k} + B_{J,k}u_k + r_k \tag{33a}$$

$$y_{J,k} = g(x_{J,k}, u_{J,k}) + e_k \approx C_{J,k}x_{J,k} + D_{J,k}u_k + e_k \tag{33b}$$

At time k, the detailed expressions of A_J, B_J, C_J, D_J and r_k in the above Equation (33) are shown in Equation (34):

$$A_{J,k} = diag[1 \quad A_{d,k}] \tag{34a}$$

$$B_{J,k} = [0 \quad B_{d,k}]^T \tag{34b}$$

$$C_{J,k} = [C_{1,k}^{R_s} \quad C_{d,k}] \tag{34c}$$

$$D_{J,k} = [0 \quad D_{d,k}] \tag{34d}$$

$$r_k = [r_k^1 \quad r_k^2] \tag{34e}$$

Similarly, assuming that both the process noise r_k and the observation noise e_k are independent white Gaussian noises with zero mean and covariance Q_r and R_e. In this paper, the specific information for the establishment of the initial values of r_k and e_k is: $r_k \sim N(0, Q_r)$, $e_k \sim N(0, R_e)$, $Q_r = 10^{-8} \times diag[1.0, 2.5, 1.0]$, $R_e = 0.000001$. And then, the covariance matrix of r_k and e_k can be expressed by the following Equation (35).

$$P_r = E(r \times r^T), P_e = E(e \times e^T) \tag{35}$$

Another issue worth noting is that since the identification of R_s is coupled in the state-space equation, $C_{1,k}^{R_s}$ in the $C_{J,k}$ matrix needs to be solved. By locating the partial derivative of the observation equation, the calculation of $C_{1,k}^{R_s}$ can be obtained as shown in Equation (36).

$$C_{1,k}^{R_s} = \frac{\partial g(x_{J,k}, u_k)}{\partial R_s}\bigg|_{R_s = \hat{R}_{s,k}^-} = \frac{\partial g(x_{J,k}, u_k)}{\partial x_{J,k}}\frac{dx_{J,k}}{\partial R_s} = \frac{dT_{ss,k}}{dR_s} = \frac{\Delta t}{R_s^2 C_s} \tag{36}$$

Then, on the time scale under fast dynamics, the joint Kalman filtering (JKF) sub-algorithm in the

high-frequency filter is used to realize the adaptive online synergistic estimation of the external thermal resistance and the internal temperature. The main iterative equations of the sub-algorithm based on JKF are as follows:

At the time $k = 0$, Initialization:

Initialize the correlation matrix of the sub-algorithm in the high-pass filter:

$$\hat{x}_{J,0}^{+} = E[x_{J,0}] \tag{37a}$$

$$P_{J,0}^{+} = E[(x_{J,0} - \hat{x}_{J,0}^{+})(x_{J,0} - \hat{x}_{J,0}^{+})^{T}] \tag{37b}$$

At the time $k = 1,2, ...$, repeat:

1. One-step prediction of the thermal characteristic state variables in fast dynamics using:

$$\hat{x}_{J,k}^{-} = A_{J,k-1}\hat{x}_{J,k-1}^{+} + B_{J,k-1}u_{k} \tag{38a}$$

$$P_{J,k}^{-} = A_{J,k-1}P_{J,k-1}^{+}A_{J,k-1}^{T} + P_{r} \tag{38b}$$

2. One-step correction of the thermal characteristic state variables in fast dynamics using:

$$K_{J,k} = P_{J,k}^{-}C_{J,k}^{T}(C_{J,k}P_{J,k}^{-}C_{J,k}^{T} + P_{e})^{-1} \tag{39a}$$

$$\hat{x}_{J,k}^{+} = \hat{x}_{J,k}^{-} + K_{k}\left(T_{sa,k} - g\left(\hat{x}_{J,k}^{-}, u_{k}\right)\right) \tag{39b}$$

$$P_{J,k}^{+} = \left(I - K_{J,k}C_{J,k}\right)P_{J,k}^{-} \tag{39c}$$

In Equations (37) to (39), $\hat{x}_{J,k}^{-}$ and $\hat{x}_{J,k}^{+}$ are the prior estimation and posterior estimation of state variables in the JKF sub-algorithm at time k, respectively; $P_{J,k}^{-}$ and $P_{J,k}^{+}$ are the prior estimation and posterior estimation of the state variable error covariance matrix at time k; $K_{J,k}$ is the Kalman gain matrix of the JKF sub-algorithm at time k; I represents the identity matrix. By combining the identification results of internal thermal characteristic parameters R_{i}, C_{i} and C_{s} shown in Equations (20) to (22), the adaptive collaborative estimation of R_{s} and T_{ia} is realized under the iterative calculation of the above JKF sub-algorithm.

3.3 Overall framework of algorithm under multi-time scale

As explained in detail above, the high-frequency characteristic parameters under fast dynamics, including ohmic resistance R_{ohm}, charge transfer resistance R_{ct}, electric double layer capacitance C_{dl}, internal heat capacity C_i, case heat capacity C_s and internal heat resistance R_i, are identified by FFRLS sub-algorithm. The low-frequency characteristic parameters under slow dynamics, including diffusion resistance R_{df} and diffusion capacitance R_{df}, are identified by the EKF algorithm. At the same time, the estimation of the thermal characteristic parameter R_s and the internal temperature is realized by the JKF algorithm specially developed. In other words, the above-mentioned multi-feature separation modeling idea naturally identifies different parameters under high-frequency dynamic and low-frequency dynamic in the high-pass filter and the low-pass filter, respectively. In this framework, each sub-algorithm of the lumped thermoelectric coupling model is developed in an independent filter, and the problems caused by the multi-time scale effects of battery model parameters are effectively alleviated. In addition, the algorithm development under the idea of multi-feature separation modeling does not introduce additional variables, and a separate driving condition is added for the identification of diffusion impedance at large time scales during modeling. Therefore, compared with the traditional thermoelectric coupling modeling at a single-time scale, the SCAAIS proposed in this paper reduces the number of iterative identifications of the diffusion impedance and reduces the computational complexity of the modeling to a certain extent. In addition, in terms of modeling accuracy, the multi-feature separation modeling idea takes into account the charge transfer and electric double-layer effects and diffusion effects inside the battery. Not only the prediction accuracy of the terminal voltage of the battery is improved, but more importantly, the physical meaning of the model parameters is made clearer. From the perspective of parameter update time, the single-time scale algorithm needs to update the parameters at each sampling step, which undoubtedly brings a large computational burden to the processor. In

contrast, the parameter update of the multi-time scale algorithm is limited by the corresponding constraints, and the computational complexity is greatly reduced. The lumped thermoelectric coupling modeling strategy proposed in this paper is implemented based on the external characteristics of the battery. Batteries of different chemical types have similar external characteristics, so the method proposed in this paper is a general thermoelectric coupling modeling method. Fig.3 shows the full framework of the strongly coupled adaptive asynchronous identification strategy and the parameter-in-the-loop correction mechanism under the idea of multi-feature separation modeling.
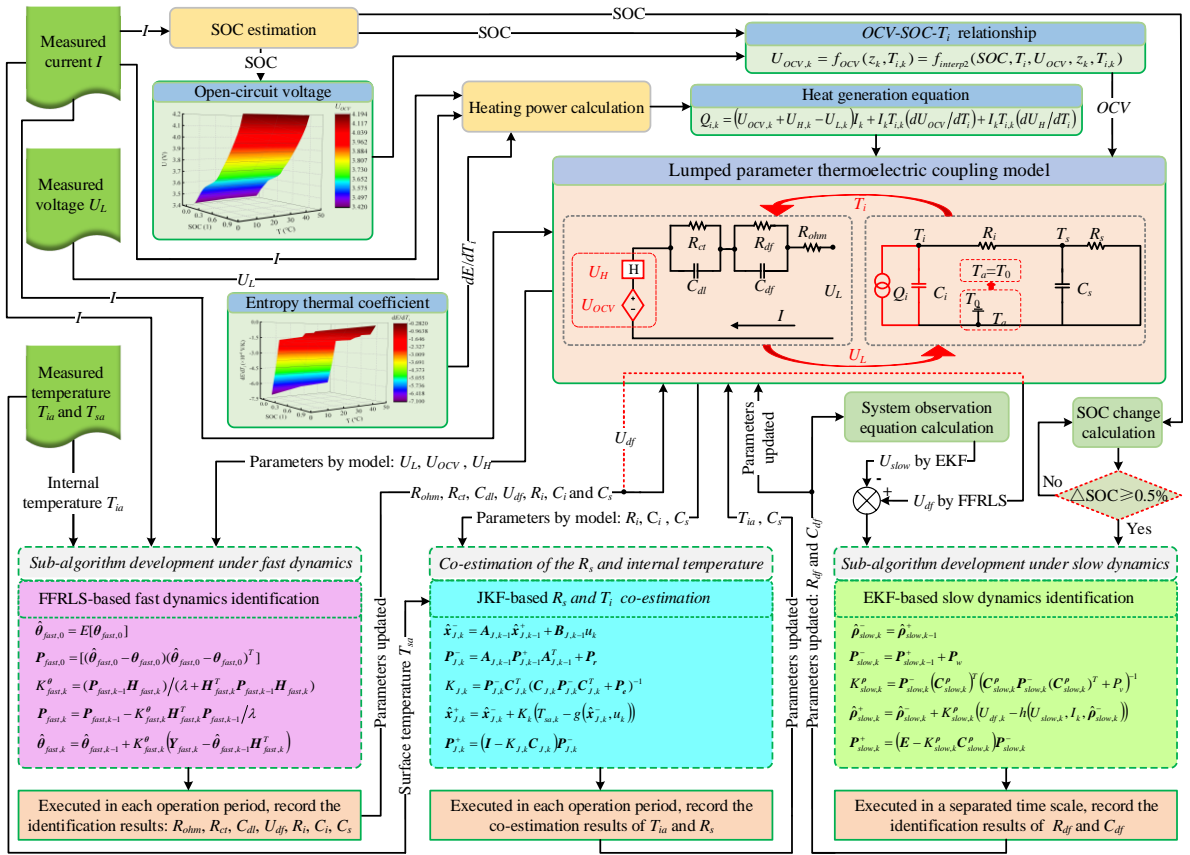
Fig. 3. Overall framework of strong coupling adaptive asynchronous identification strategy

From Fig. 3, the in-loop correction mechanism of each parameter under the strongly coupled asynchronous representation strategy can be clarified. It should also be clarified that in the implementation of the high-pass filter and the low-pass filter, we set the low-frequency parameters to remain unchanged while the fast dynamics sub-algorithm is being executed. In other words, the diffusion

voltage U_{df} is used as one of the parameters to be identified in the high-frequency sub-algorithm. In the implementation of the sub-algorithms, the two high-pass filters under the fast dynamics are executed under each sampling period of the system, while the low-pass filter under the low-frequency dynamics is only executed under a specific sampling period that meets certain conditions. This scheme has at least two obvious advantages: first, it can reduce the dispersion of model parameters and improve the consistency of model parameters; second, it can reduce the data calculation and storage burden of the electronic control unit in the BMS, and improve the efficiency of embedded applications.

4 Experiments and results analysis

4.1 Experimental platform and procedure

In order to determine the parameters of the proposed lumped thermoelectric coupling model, and also to verify the accuracy of the model and the precision of the proposed SCAAIS, the test platform is built with a commercial LiFePO$_4$ battery model HTCNR18650 as the experimental sample. It should be pointed out that the modeling of thermoelectric coupling at the battery pack level is inseparable from the overall development of the thermal management system. In addition, the thermoelectric coupling modeling research at the battery pack level needs to take into account the consistency of the battery. Therefore, the current study does not provide a more detailed comparison of the modelling of lumped thermal properties at the battery pack level. Due to the many similarities in the external characteristics between the battery pack and the battery samples, such as OCV-SOC relationship, charge transfer and electric double-layer effect, diffusion effect, etc. Therefore, the method proposed in this paper is also applicable to the thermoelectric coupling modeling work at the battery pack level. The main equipment in the test platform includes a host for recording experimental data, a thermostat for controlling ambient temperature, and a battery test system for controlling current and voltage. In addition, the data

measurement accuracy of the battery testing equipment in the experimental platform is one ten thousandth. Since the corresponding OCV values differ by approximately 80 mV to 120 mV when the SOC varies by 0.5%. Therefore, the accuracy of this data measurement can also meet the requirements. The standard capacity and voltage of the battery samples are 2200 mAh (1 C) and 3.6 V, respectively. The discharge cut-off voltage and the charge cut-off voltage at 0.5 C are 2.5 V and 4.2 V, respectively. The working temperature of the sample in the charged state is in the range of 0°C to 55°C. The connections between the devices in the test platform and the detailed characteristic parameters of the test samples are shown in Fig. 4(a) and (b), respectively.
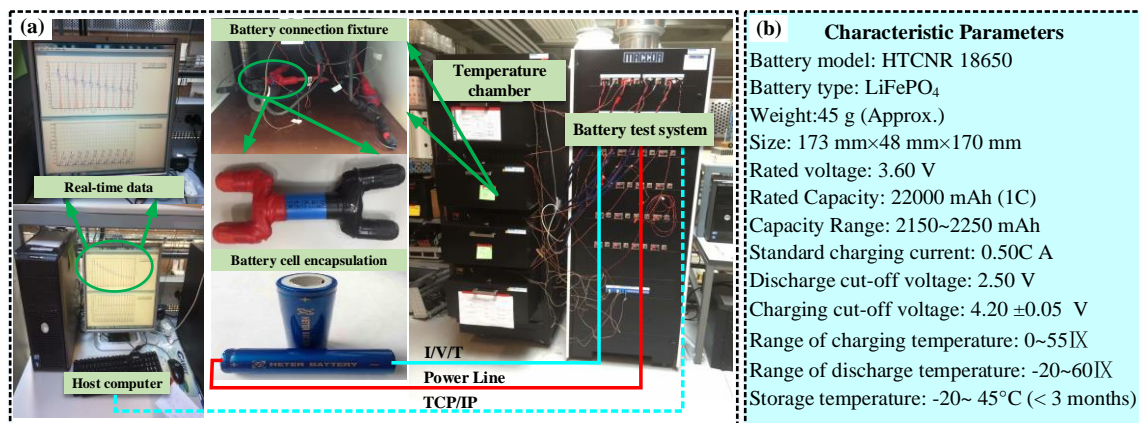
Fig. 4. (a) Experimental platform; (b) Battery characteristic parameters.

Before the test, the high-precision temperature sensor is connected to the electrode lug of the battery sample, and sealed with special electrical tape with high temperature resistance, insulation and heat insulation. At this time, the temperature value measured by the high-precision temperature sensor can be regarded as the internal temperature value of the battery. Then, the sealed battery sample is fixed in the incubator with a special fixture, and the electrode is connected to the battery testing system connected to the host to complete the preparation before the experiment. Further, in order to determine the coupling relationship of the related parameters in the thermal characteristic sub-model and the electrical characteristic sub-model, the hybrid pulse power characteristic cycle (HPPCC) test and the full-charge and full-discharge test (FCFDT) are designed at three different temperatures, namely 5 ℃, 25 ℃, and 45 ℃. Due to the experimental setup of cyclic working conditions, the duration of each working condition is relatively long. Therefore, in the experiment, the sampling frequency of the charge-discharge phase

and the short-term shelving phase (10 s for HPPCC) is set to 1 s, and the long-term shelving phase (2 hours for HPPCC, 1 hour for FCFDT) is set to 30 s. Under the setting of this mixed sampling frequency, the post-processing problem caused by the huge data set is solved, and it can also provide corresponding evidence that the method has no special requirements for the frequency of data measurement. The detailed steps of HPPCC experiment and FCFDT experiment are shown in Fig. 5(a) and (b), respectively.
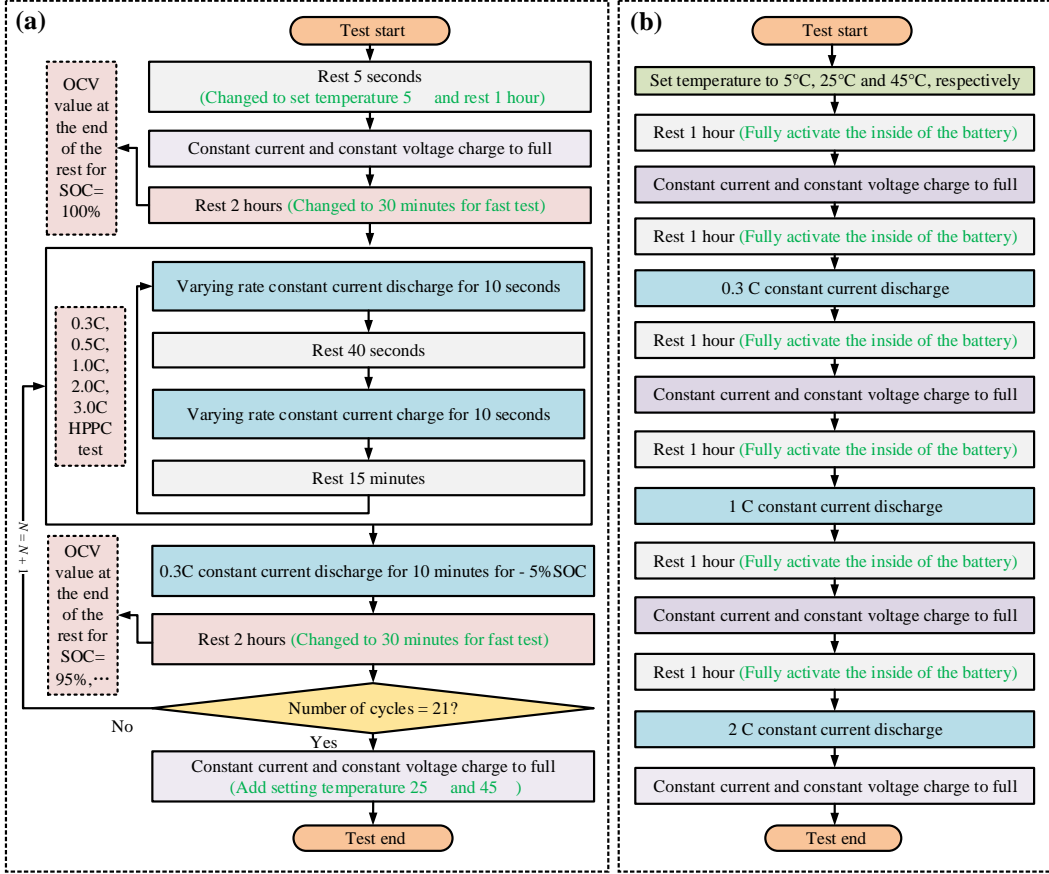

Fig. 5. Experimental steps of HPPCC and FCFDT at different temperatures: (a) HPPCC; (b) FCFDT

When conducting HPPCC and FCFDT experiments at different temperatures, the battery is first placed in an incubator with a set temperature for 1 hour, so that the battery's own state and the test environment reached a temperature equilibrium. Then, uniformly use a current input of 0.3 C to charge the battery with constant current and constant voltage until it is fully charged. At this time, HPPCC and FCFDT can be carried out respectively. HPPCC adopts the current pulse sequence of 0.5 C, 1.0 C, 2.0 C and 2.0 C to realize the charge-discharge test in a small cycle, which does not reduce the SOC value of the battery at this stage. Further, the battery is discharged with a current pulse of 0.3 C for 10 minutes

to reduce the SOC value of the battery by 5%. Repeat the above small cycle to achieve the acquisition of HPPCC full sequence data at different temperatures. The HPPCC experimental results are shown in Fig. 6(a) to (c). Similar to the above idea, the FCFDT experiment set three different Current ratios (Cr), namely 0.3 C, 1 C and 2 C, under the same ambient temperature, and performed constant current discharge on the battery samples until the cut-off voltage is 2.5 V. A more detailed analysis of the experimental steps can be found in our previous work [50]. The discharge experiments at different rates are repeated to obtain the full sequence data of FCFDT at different temperatures. The results of the FCFDT experiments are shown in Fig. 6(d) to (f).
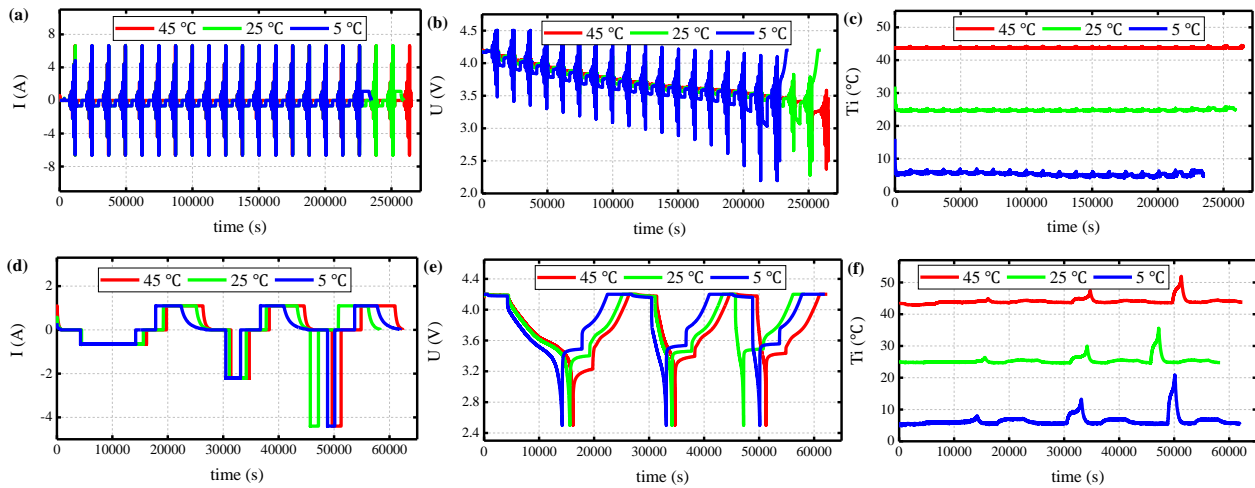
Fig. 6. Experimental results: (a) Current under HPPCC; (b) Voltage under HPPCC; (c) Temperature under HPPCC; (d) Current under FCFDT; (e) Voltage under FCFDT; (f) FCFDT temperature below.

4.2 Model-based thermoelectric parameters identification results

4.2.1 Electrical parameters consider multi-time scales

In order to realize the online parameter identification of the lumped thermoelectric coupling model based on the SCAAIS, it is necessary to determine the relevant parameter values in the modeling through experiments in advance. The battery capacity values at different discharge rates can be obtained by FCFDT at different temperatures. By further normalizing the discharge rate with the standard capacity,

the actual capacity value of the battery sample at each discharge rate and internal temperature can be obtained. Through the HPPCC experiment, the OCV values of the battery at every 5% SOC at different temperatures can be obtained. Considering the influence of the hysteresis effect of the LiFePO4 battery samples, this paper uses the OCV-SOC data at different temperatures to establish a three-dimensional table, and obtains the hysteresis voltage through the interpolation function. In addition, the entropy thermal coefficient is an important parameter in the thermoelectric coupling model of the battery, which is used to calculate the heat production of the internal chemical reaction of the battery. In the acquisition of this parameter, this work takes 11 different SOC values (every 10% SOC), and uses the derivative of optimized OCV to temperature to calculate the entropy thermal coefficient at different temperatures. The three-dimensional experimental data of each parameter at different temperatures are shown in Fig. 7.
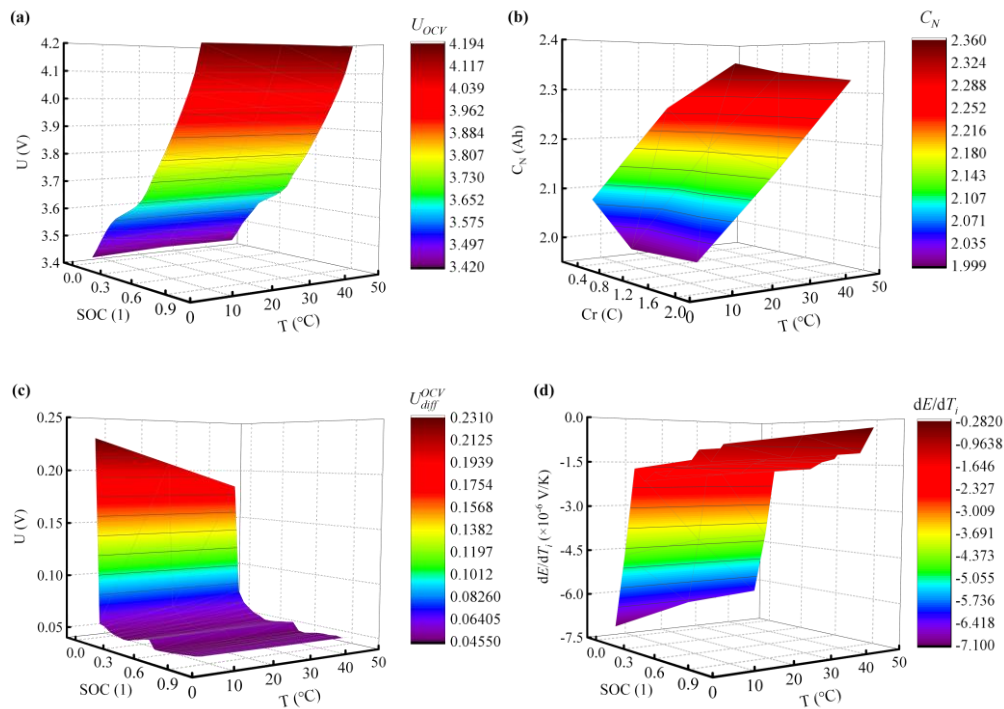
Fig. 7. Experimental results of parameters at different temperatures: (a) U_{OCV}-SOC-T_i; (b) C_N-C_r-T_i; (c) U_{diff}^{OCV}-SOC-T_i; (d) dE/dT_i-SOC-T_i.

In this work, the FFRLS algorithm and the EKF algorithm are coupled to identify the electrical

characteristic parameters of the lumped thermoelectric coupling model. Affected by the multi-time scale effect of impedance parameters, the FFRLS algorithm is used for the identification of high-frequency characteristic parameters, and the EKF algorithm is used for the identification of low-frequency parameters. In addition, the composite pulse current distribution contained in the HPPC case is beneficial to the parameter identification of the battery model, which has been proved in many literatures [54, 55]. In view of this, this paper also carried out the online parameter identification of the lumped thermoelectric coupling model under the HPPCC test. At this time, based on SCAAIS, combined with the HPPCC experimental data shown in Fig. 6 and the experimental data at different temperatures shown in Fig. 7, the electrical characteristic parameters of the lumped thermoelectric coupling model are iteratively calculated, as shown in Fig. 8.
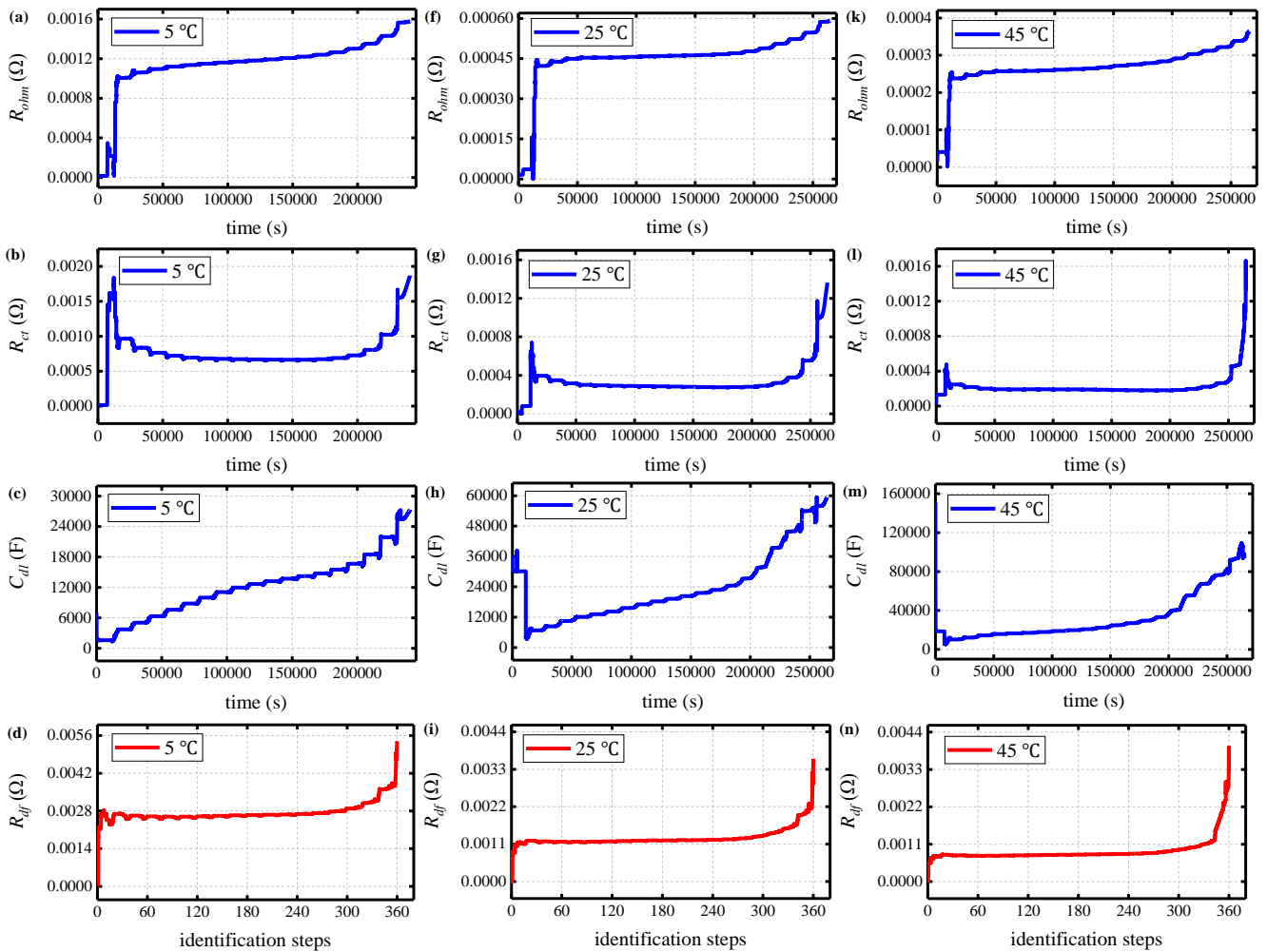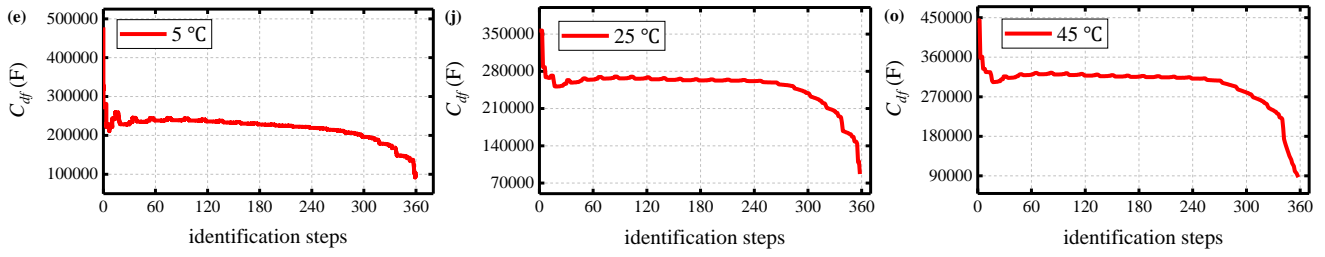
Fig.8. Identification results of electrical characteristic parameters at different temperatures: (a-e) 5 ℃; (f-j) 25 ℃;

(k-o) 45 ℃.

As can be seen from Fig. 8, since the multi-time scale effect of impedance parameters is considered in the thermoelectric coupling modeling, the identification result curve of the diffusion impedance $R_{df}C_{df}$ replaces the traditional time axis with the identification step size. From the identification results, it can be seen that the temperature has a strong correlation with the model parameters. Among them, with the increase of temperature, the resistance values of ohmic internal resistance R_{ohm}, charge transfer resistance R_{ct} and diffusion resistance R_{df} show an increasing trend, while the values of electric double layer capacitor C_{dl} and diffusion capacitor C_{df} show a decreasing trend. In addition, it can be found that the ohmic internal resistance Rohm, the charge transfer resistance and the diffusion resistance at the end of the discharge are slightly larger than the resistance in the early and middle stages of the discharge. The main reason for the above phenomenon is the reduction of active substances inside the battery at low power or low temperature. The correlation between battery parameters and temperature reported here is consistent with the trend reported in Ref. [32]. These phenomena are consistent with the external characteristics of the battery, which can preliminarily indicate that the parameter identification results of the lumped thermoelectric coupling model based on SCAAIS have strong rationality.

4.2.2 Thermal parameters and robustness analysis

Similarly, the identification of thermal characteristic parameters in the lumped thermoelectric coupling model is carried out based on the HPPCC test data results. Since the internal thermal characteristic parameters of the battery are related to the material of the battery itself, its value remains

almost unchanged during the use of the battery. Therefore, the average values of the identification results

of the internal thermal resistance R_i, the internal thermal capacity C_i and the case thermal capacity C_s

are 1.78 °C/W, 138.62 J/°C and 0.59 J/°C under HPPCC experiments at different temperatures,

respectively. It is worth noting that the external thermal resistance R_s in the embedded battery system

is greatly affected by the external heat transfer coefficient and needs to be considered separately. In this

work, HPPCC experiments at different temperatures are all carried out in the same incubator, so that the

external convection environments under different experimental groups are basically the same. This same

convective environment leads to two results: first, the external thermal resistance R_s remains basically

unchanged; second, the battery surface temperature after the algorithm converges is approximately equal

to the ambient temperature. In this case, based on the HPPCC experiments at different temperatures, the

convergence results of the external thermal resistance results at 5 °C, 25 °C, and 45 °C can be obtained

as 8.65 °C/W, 7.69 °C/W and 7.21 °C/W, respectively. It can be found that although under the same

external convection environment, there is still an error in the convergence value of the external thermal

resistance R_s at different ambient temperatures, which shows the importance of identifying R_s

separately.

Another important point is that the external thermal resistance R_s of the model cannot be obtained

in advance in the application. Therefore, different from most studies, the effect of the R_s initial value

on the model stability and robustness is discussed in this work. Specifically, on the basis of the HPPCC

experiment, different initial values of the R_s are set to verify the stability and convergence of the model.

The experimental results are shown in Fig. 8. Set the initial value of R_s to 1 ℃/W, 10 ℃/W, 20 ℃/W,

30 ℃/W, and 40 ℃/W respectively in the experiments. It should be noted that, in view of the amount of

data amplified by HPPCC, we only show the experimental data of the first 3 hours of the HPPCC

experimental. If the convergence time is defined as the time when the difference between the maximum

and minimum values of R_s identified under different initial values does not exceed 1 °C/W. Then from the results shown in Fig. 9(a-2) to (c-2), the convergence time of the external thermal resistance R_s can be obtained as 1185 s, 982 s and 171 s at 5 °C, 25 °C and 45 °C, respectively. And the maximum fluctuation of the R_s value after convergence does not exceed 0.6 °C/W. The results show that the model has high stability and robustness, and can quickly cope with the unknown initial value of the external thermal resistance.
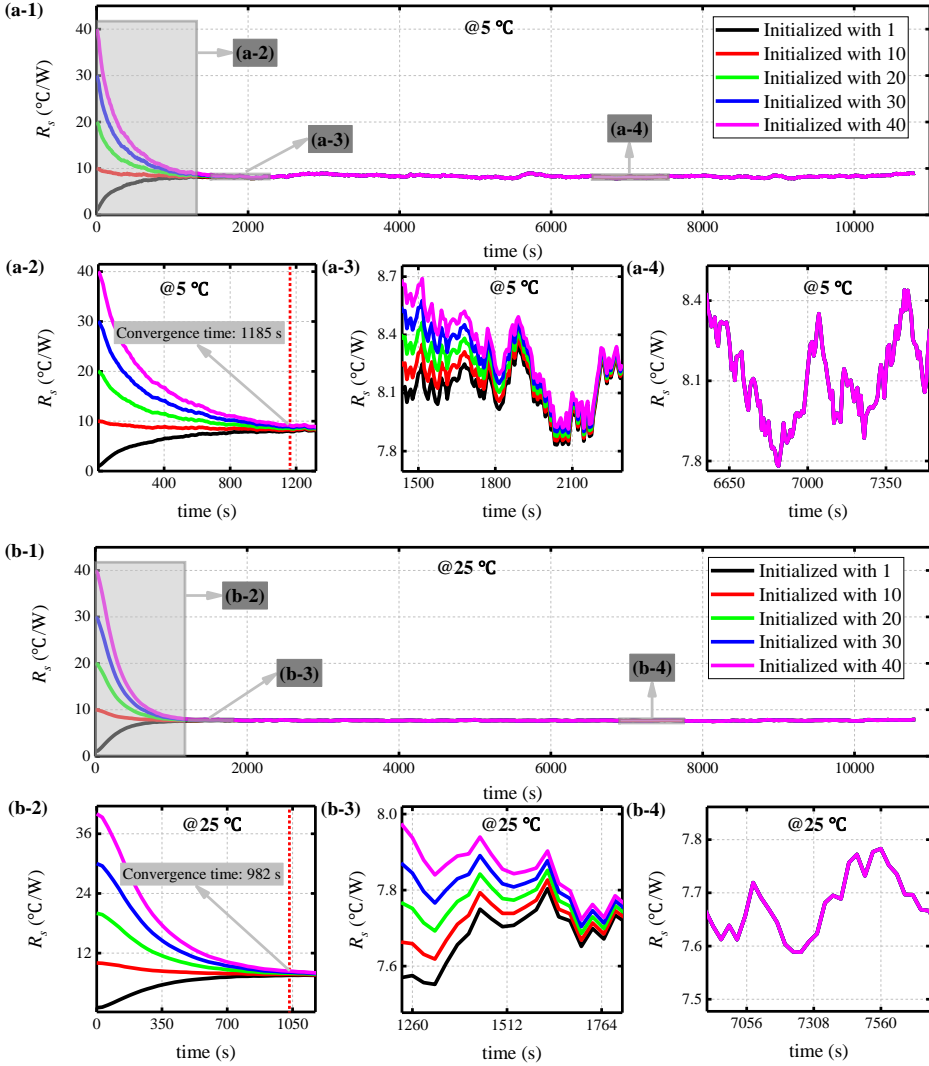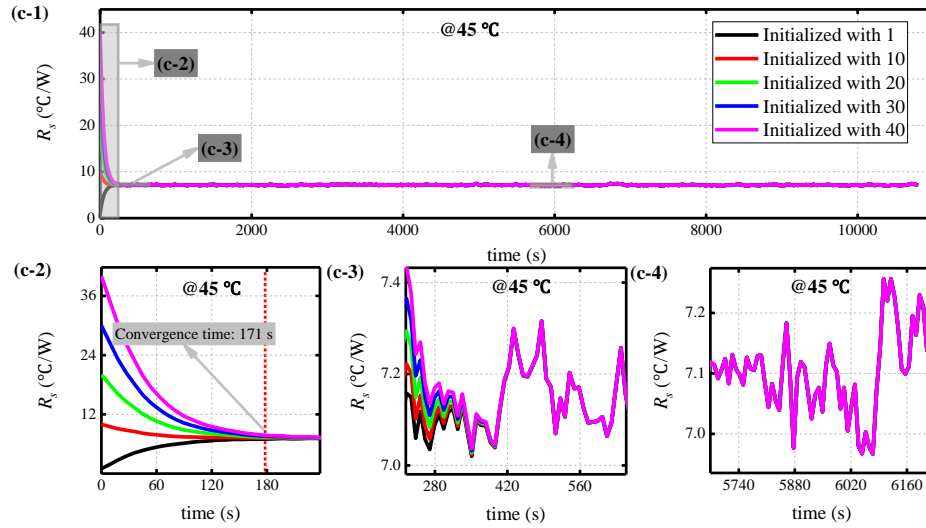
Fig. 9. Variation curve of R_s under different initial values: (a) 5 ℃; (b) 25 ℃; (c) 45 ℃.

4.3 Accuracy verification of the proposed model and method

4.3.1 Analysis of internal temperature prediction results

Accurate internal temperature estimation is the primary factor in preventing thermal runaway and ensuring the safe use of the battery. In this work, the internal temperature is used as one of the parameters to be identified in the thermoelectric coupling model, and the estimation result is used to correct parameters such as battery capacity and open circuit voltage. In order to verify the accuracy of the lumped thermoelectric coupling model in characterizing thermal characteristics, and the accuracy of the proposed SCAAIS for internal temperature estimation, the HPPCC and FCFDC conditions are performed on commercial battery samples at different temperatures. Using the identification results of thermal characteristic parameters, the iterative calculation of internal temperature based on SCAAIS is realized at different temperatures. The internal temperature estimation results of HPPCC and FCFDC under different temperatures are shown in Fig. 10 and Fig. 11, respectively.
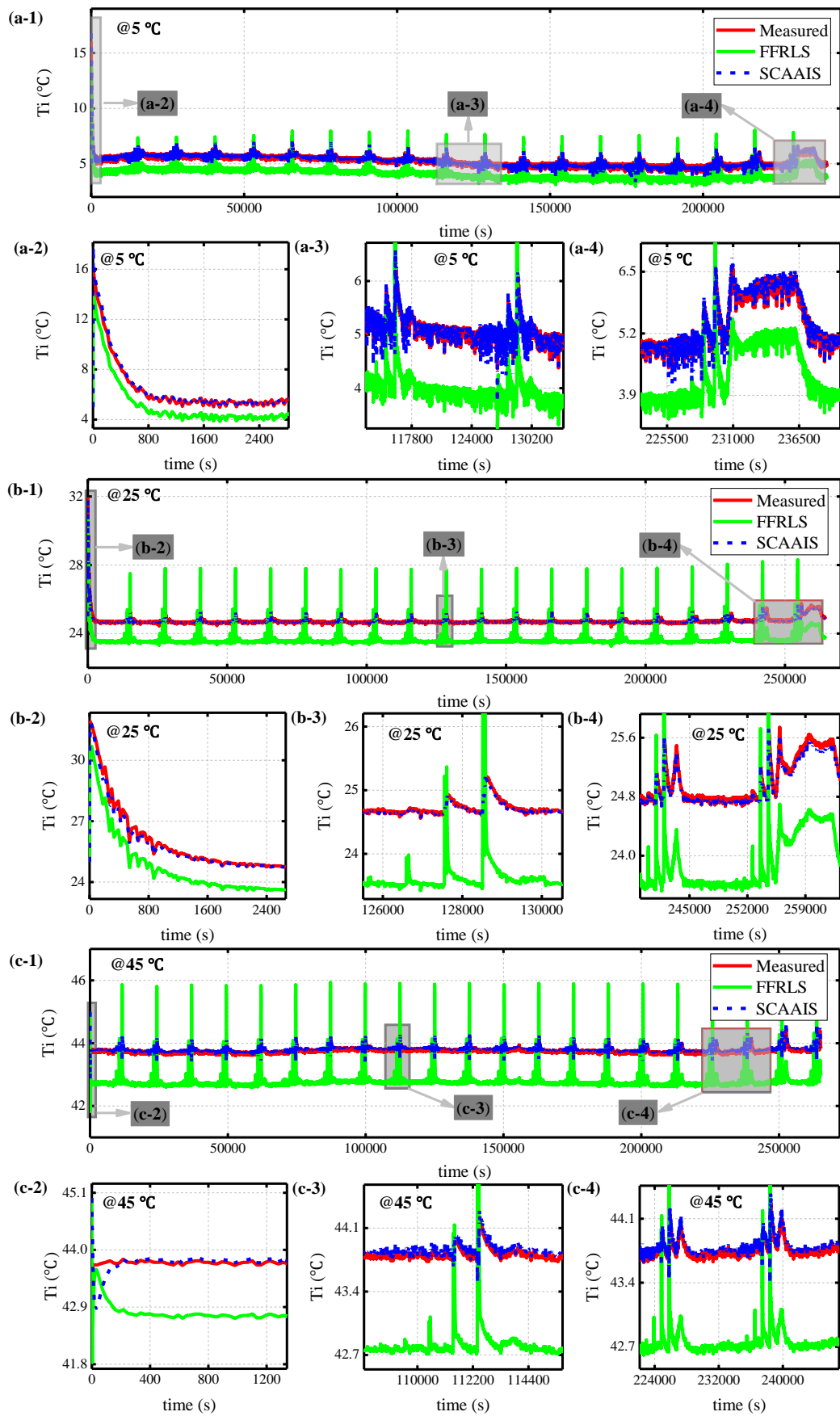
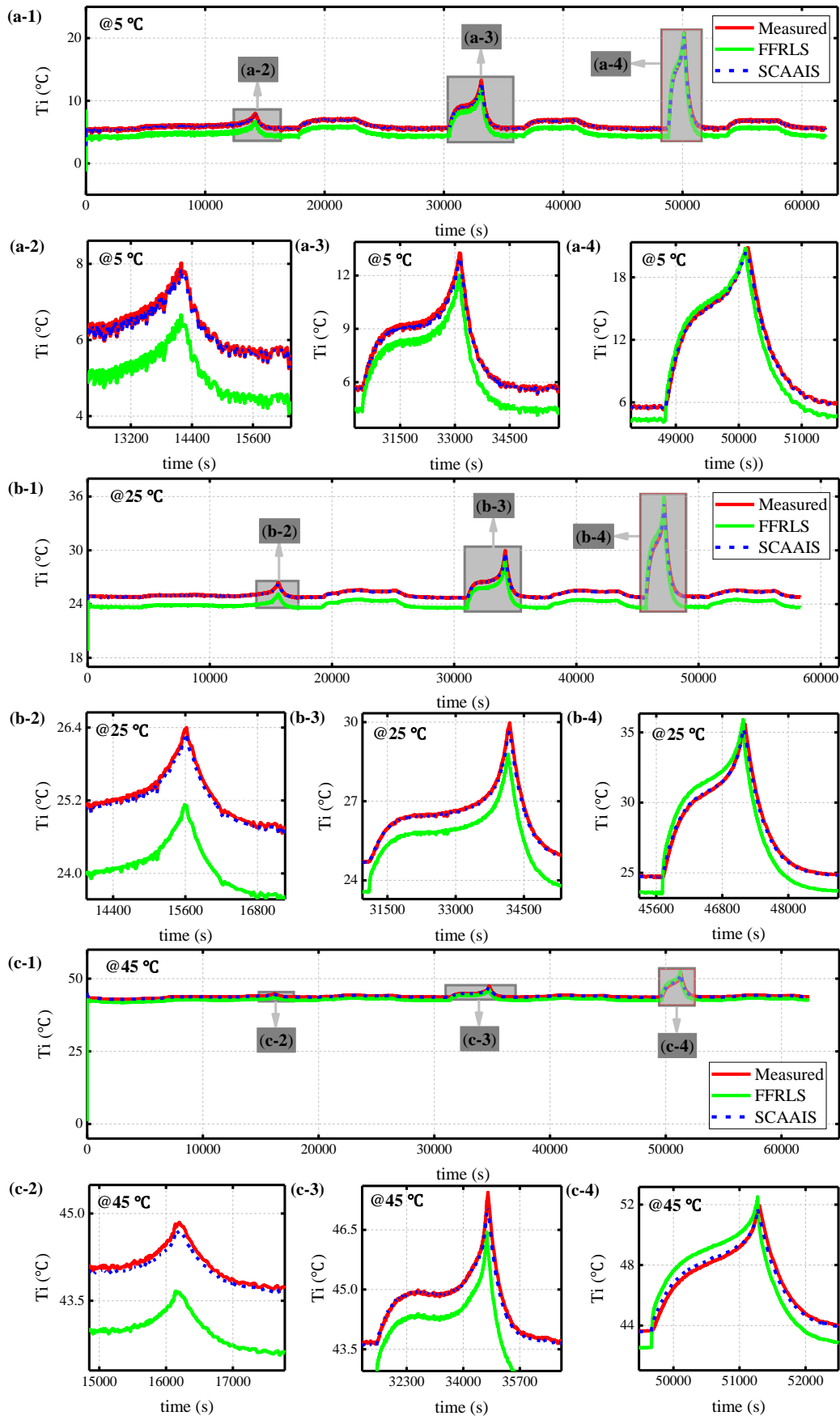Fig. 10. Estimated results of internal temperature under HPPCC: (a) 5 ℃; (b) 25 ℃; (c) 45 ℃.

Fig. 11. Estimated results of internal temperature under FCFDT: (a) 5 ℃; (b) 25 ℃; (c) 45 ℃.

In Fig. 10 and Fig. 11, the prediction results under both experimental conditions show that not

considering the uncertainty of the external thermal resistance R_s will lead to an offset error in the estimation of the internal temperature of the battery. This error will continue throughout the battery use process, and is more obvious and transferable in the actual use of the battery. In other words, the offset error will cause inaccurate calculation of battery capacity and OCV, which will make the internal temperature correction function ineffective, and even lead to system divergence. Comparing the estimation results under the two strategies, it can be found that the internal temperature prediction results under the proposed SCAAIS can better track the measured value of the internal temperature of the battery, and better solve the problem of offset error. In order to visually show the estimation effect under different working conditions, the estimation error of internal temperature under different methods is calculated. The results of the internal temperature estimation error under HPPCC and FCFDC conditions are shown in Fig. 12 and Fig. 13, respectively.
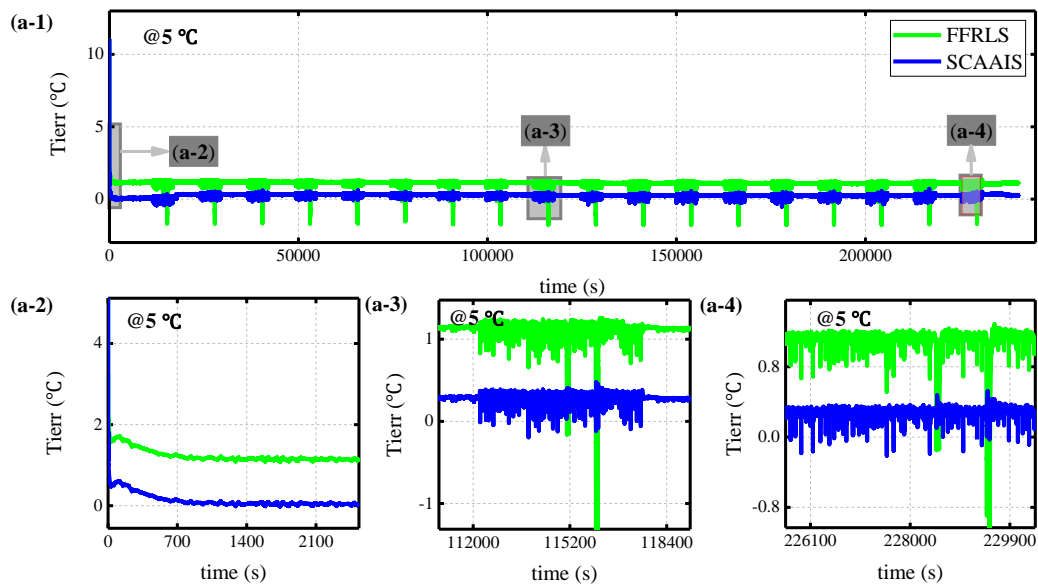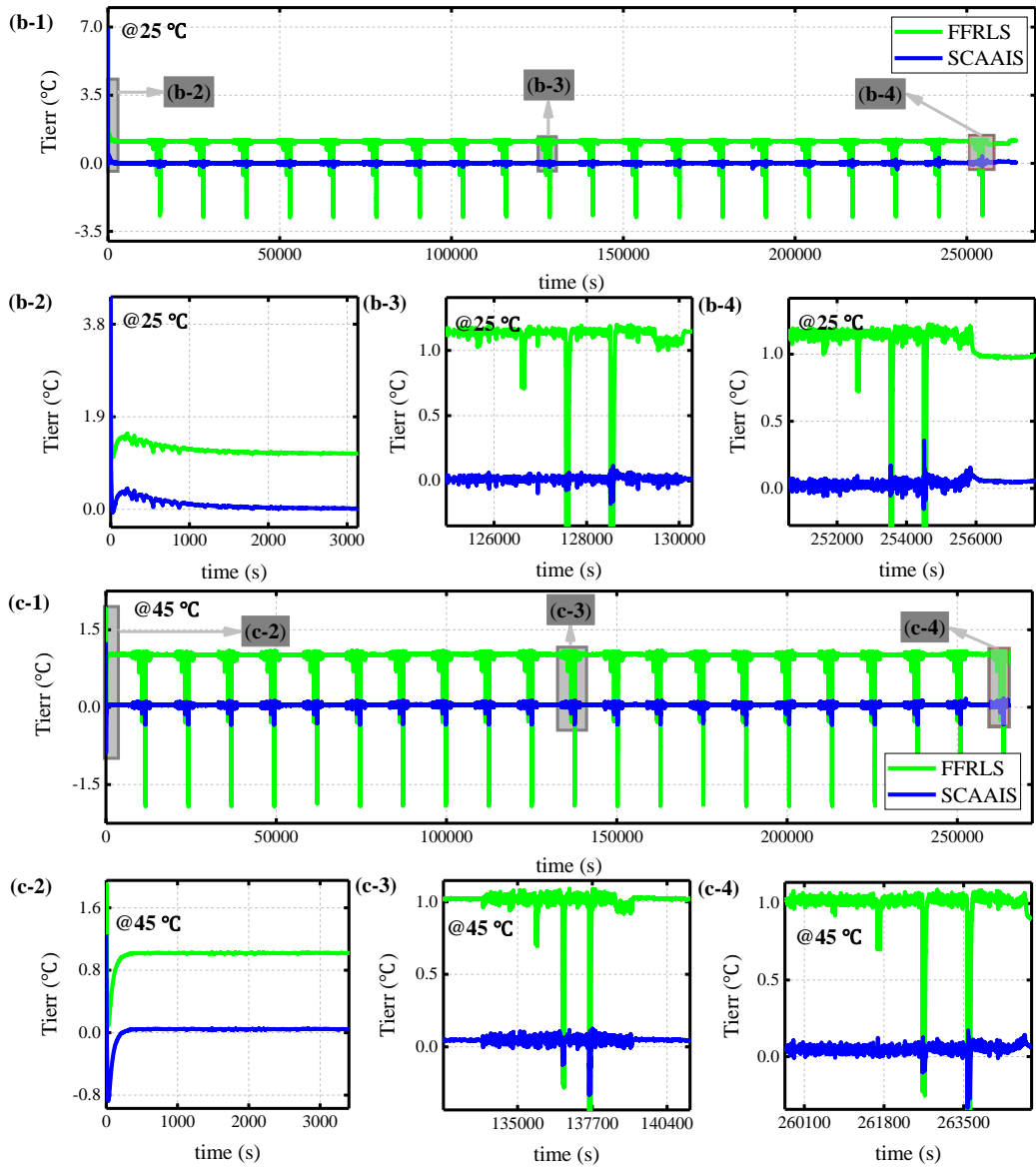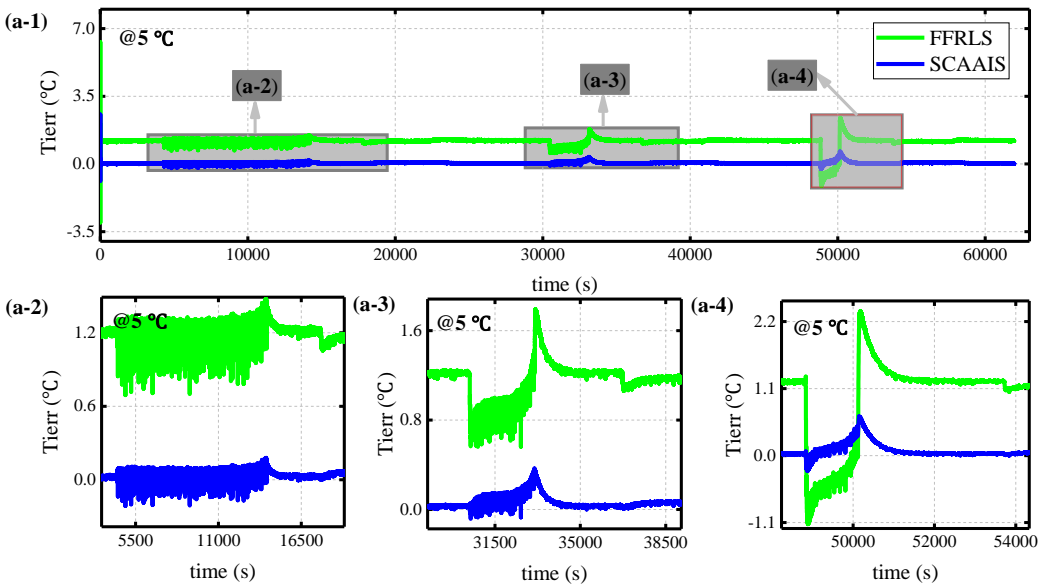
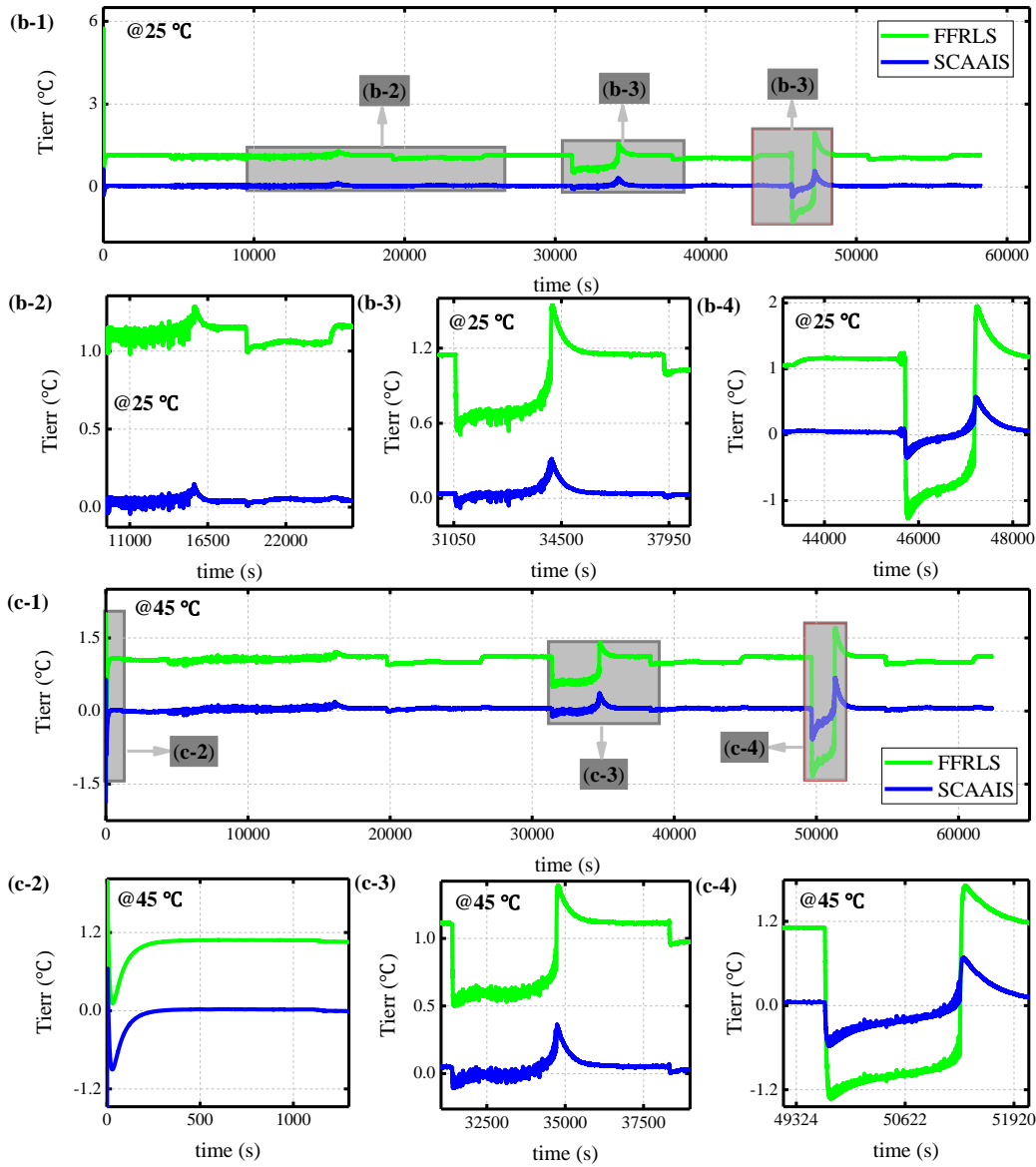Fig. 12. Estimation error of internal temperature under HPPCC: (a) 5 ℃; (b) 25 ℃; (c) 45 ℃.

Fig. 13. Estimation error of internal temperature under FCFDT: (a) 5 ℃; (b) 25 ℃; (c) 45 ℃.

In Fig. 12 and Fig. 13, it can be seen that the internal temperature estimation errors under different prediction methods are mainly manifested when the battery is excited by current pulses. Using the FFRLS method without considering the uncertainty of R_s, the fluctuation of the estimation error under different temperature conditions exceeds 3 °C. Based on the proposed SCAAIS, the fluctuation of the estimation error for different temperature conditions does not exceed 0.5 °C. In addition, in combination with Fig. 9, it can be found that with the increase of the amount of data, the external thermal resistance gradually converges, so that the estimation error of the internal temperature decreases accordingly. The calculation results of more intuitive quantitative indicators root-mean-square error (RMSE) and mean

absolute error (MAE) are shown in **Table 1**.

Table 1 RMSE and MAE for thermal characteristics sub-model under different operating conditions

	HPPCC					
	5 ℃		25 ℃		45 ℃	
	FFRLS	SCAAIS	FFRLS	SCAAIS	FFRLS	SCAAIS
RMSE (℃)	1.134	0.276	1.132	0.031	1.011	0.049
MAE (℃)	1.130	0.262	1.127	0.023	1.008	0.046
	FCFDT					
	5 ℃		25 ℃		45 ℃	
	FFRLS	SCAAIS	FFRLS	SCAAIS	FFRLS	SCAAIS
RMSE (℃)	1.200	0.081	1.091	0.064	1.039	0.091
MAE (℃)	1.186	0.058	1.081	0.049	1.029	0.061

Observing the quantitative calculation results shown in **Table 1**, it can be found that the RMSE and MAE of the SCAAIS method are higher than those of the traditional FFRLS method under different working conditions. Among them, the RMSE of internal temperature estimation error under the HPPCC experiment at 5 ℃, 25 ℃ and 45 ℃ is decreased by 0.858 ℃, 1.101 ℃, 0.962 ℃, and the MAE accuracy is decreased by 0.868 ℃, 1.104 ℃, 0.962 ℃. The RMSE of internal temperature estimation error under the FCFDT experiment at 5 ℃, 25 ℃ and 45 ℃ is decreased by 1.119 ℃, 1.027 ℃, 0.948 ℃, and the MAE decreased is decreased by 1.128 ℃, 1.032 ℃, 0.968 ℃. One of the main reasons for this result is that the uncertainty of R_s is considered in the SCAAIS method, so that the algorithm can adaptively match the current battery usage environment, thereby improving the estimation accuracy of the internal temperature. It provides guarantee for correcting battery capacity and open circuit voltage parameters.

4.3.2 Verification of terminal voltage tracking effect

The prediction effect of terminal voltage is an important reference for judging the accuracy of battery modeling, and its prediction result affects the estimation accuracy of the internal state in the BMS. In order to verify the terminal voltage tracking effect of lumped thermoelectric coupling modeling, HPPCC conditions are first performed on commercial LiFePO₄ battery samples at different temperatures. Using the parameter identification results under HPPCC and the accurate internal temperature estimation

results, the terminal voltage iterative calculation based on the SCAAIS is realized. Fig. 14 and Fig. 15

show the online tracking results of the battery terminal voltage under HPPCC and FCFDC conditions at
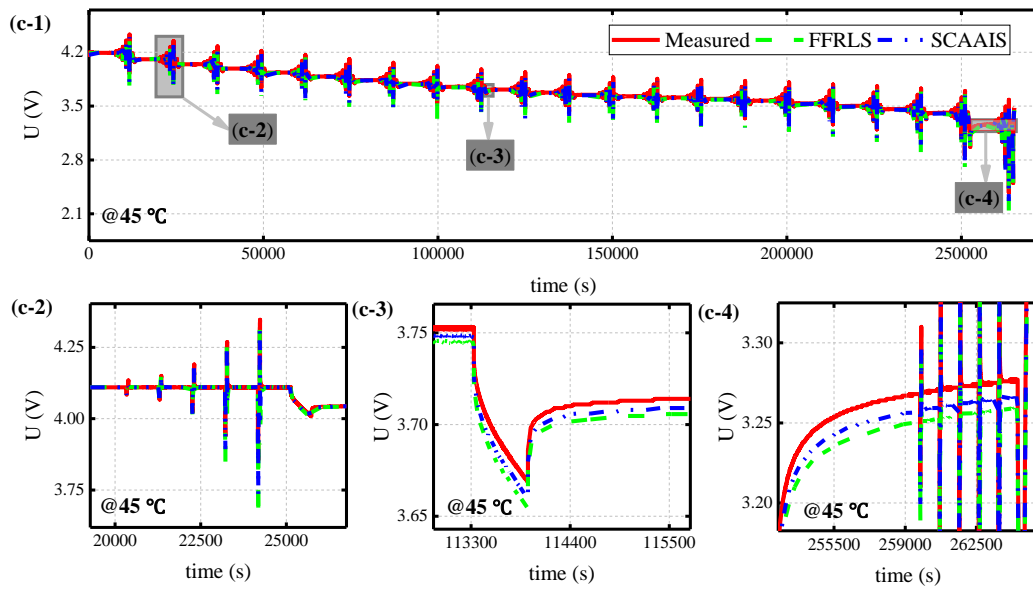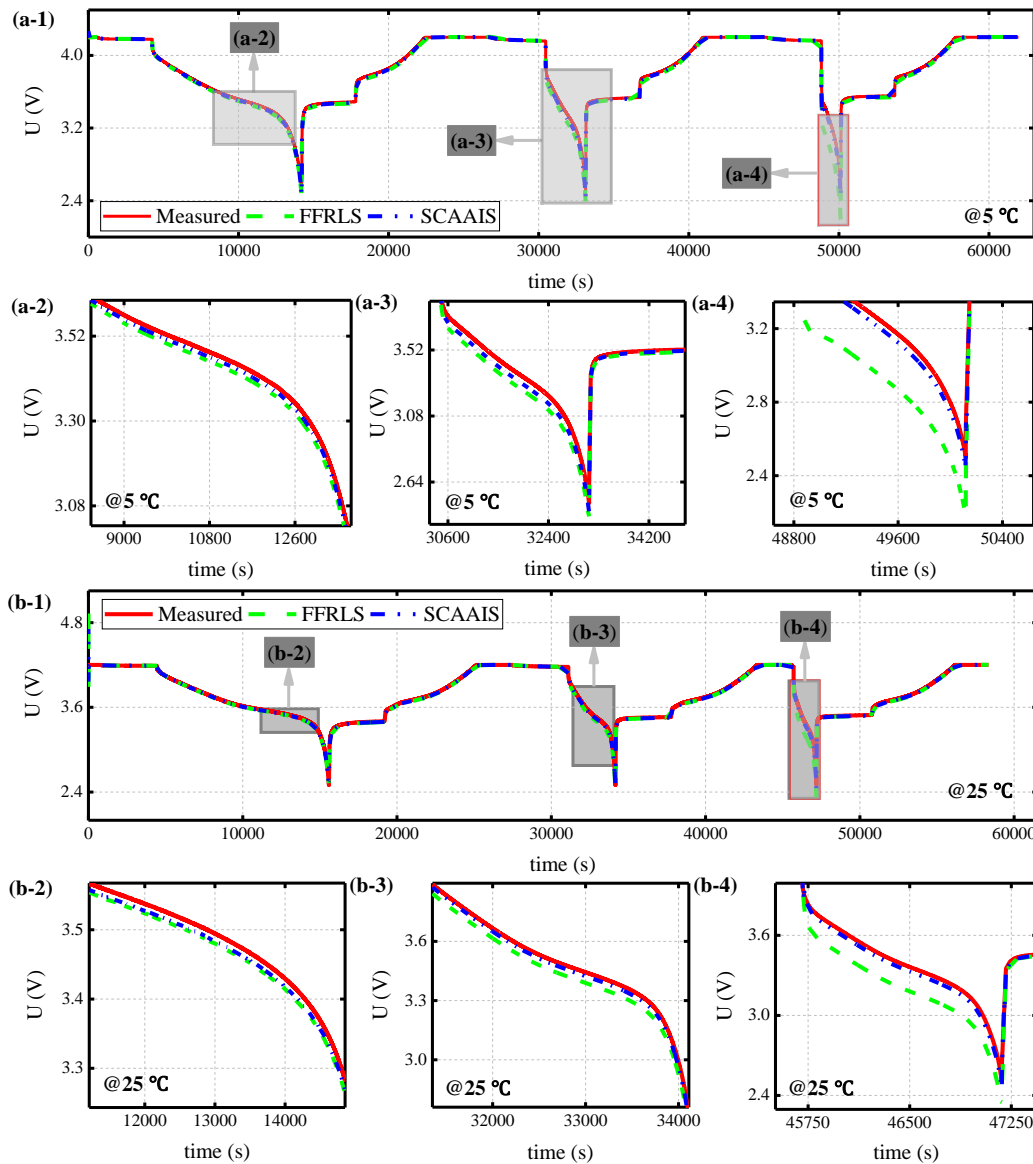
different temperatures, respectively.
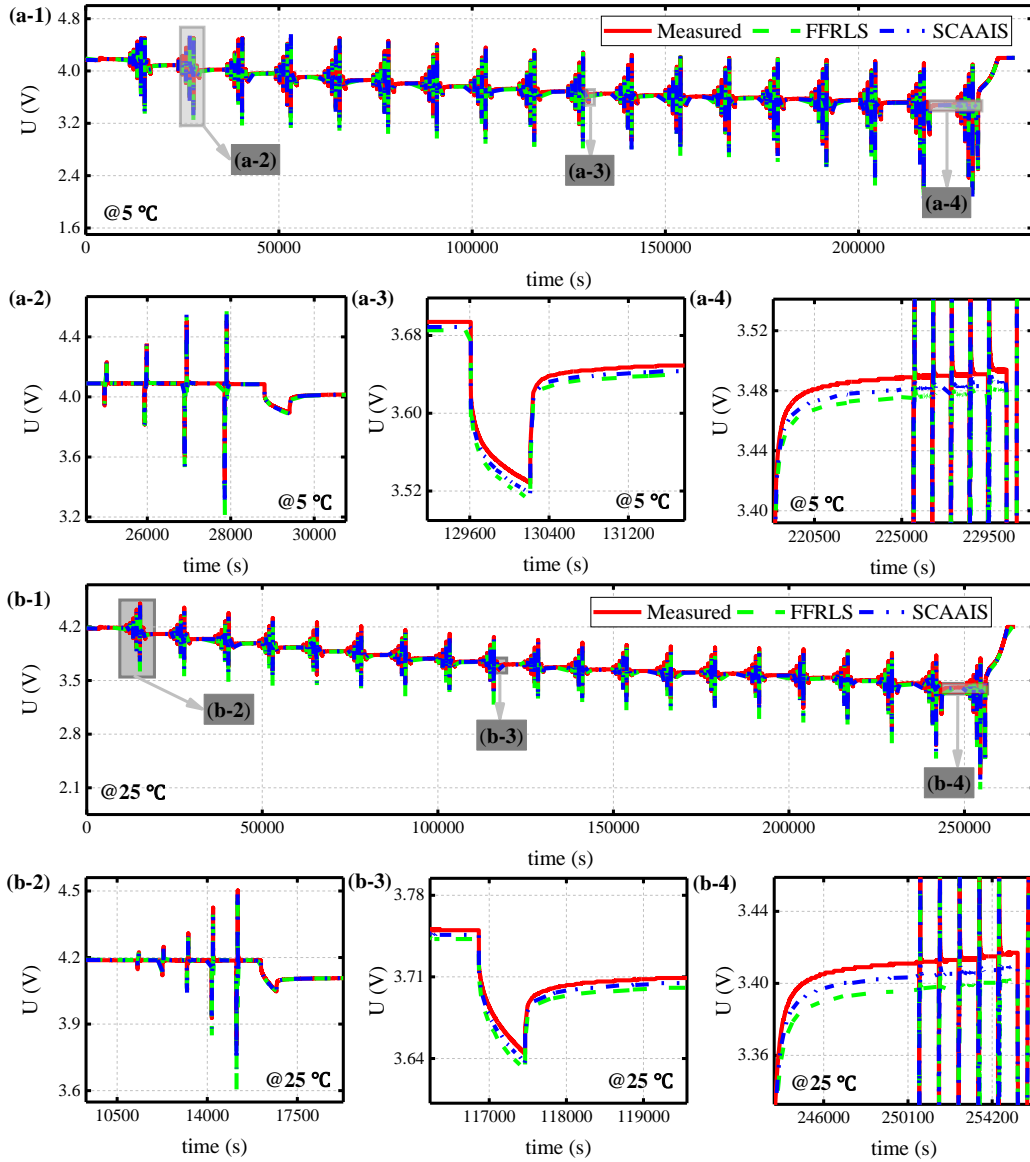
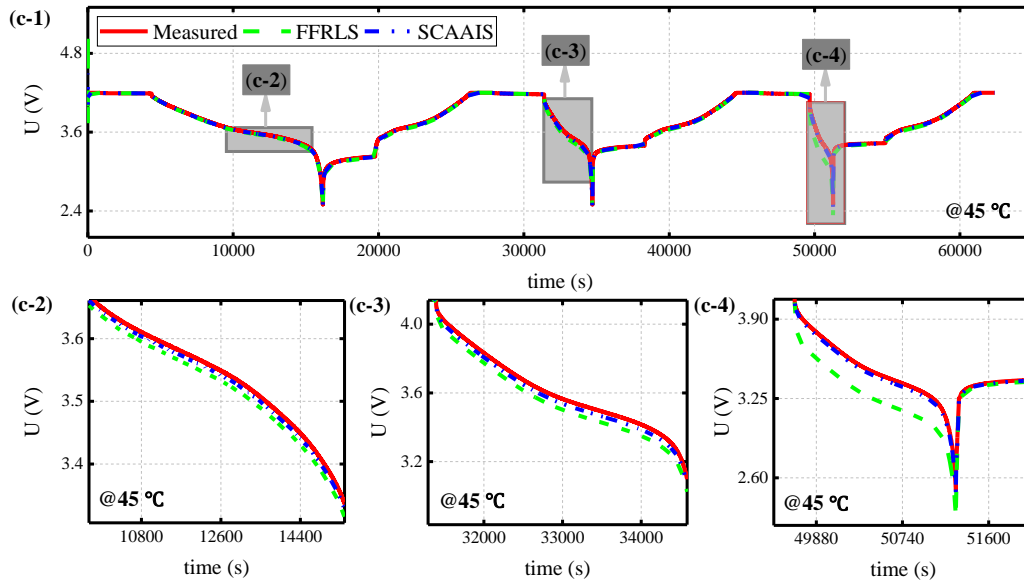Fig. 14 Estimated terminal voltage under HPPCC condition: (a) 5℃; (b) 25℃; (c) 45℃

Fig. 15 Estimated terminal voltage under FCFDC condition: (a) 5℃; (b) 25℃; (c) 45℃.

Observing Fig. 14 and Fig. 15, it can be seen that the terminal voltage prediction results based on the proposed SCAAIS are better than the terminal voltage tracking effect under the traditional FFRLS method, especially in sub-Fig. 14(a/b/c-3) and sub Fig. 15(a/b/c-4) shown in the long discharge phase. This is attributed to the multi-feature separation modeling idea in SCAIS, which enables accurate characterization of the diffusion impedance of the battery at low frequencies. In addition, accurate internal temperature estimation makes high-precision battery OCV and capacity values available, thereby improving the iterative calculation accuracy of SCAAIS. Similarly, in order to visually show the tracking effect of the battery terminal voltage under different working conditions, the terminal voltage prediction error based on different estimation methods is calculated. The results of terminal voltage prediction error under HPPCC and FCFDC conditions are shown in Fig.16 and Fig.17, respectively.
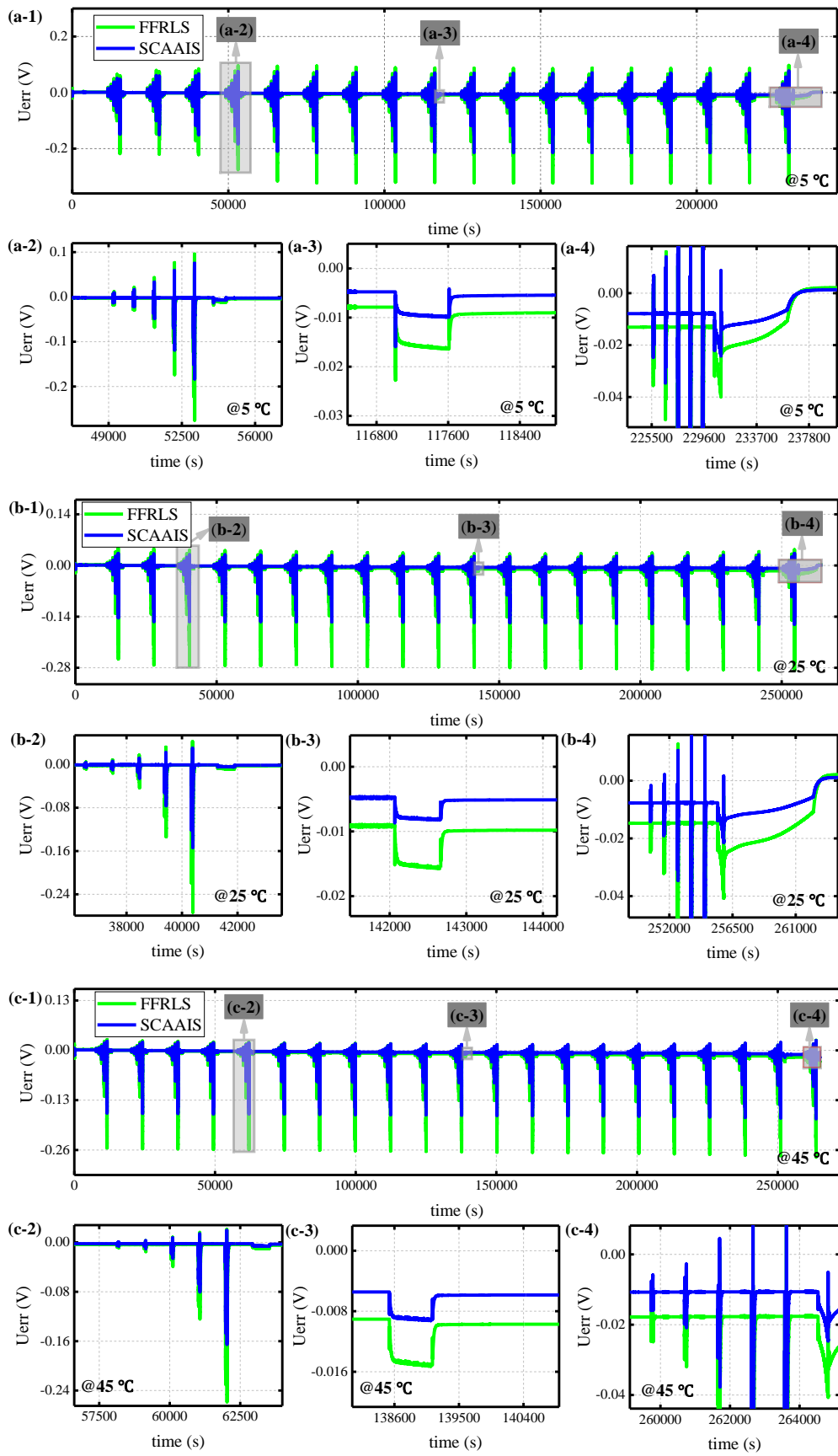
Fig. 16. Terminal voltage prediction error under HPPCC: (a) 5 ℃; (b) 25 ℃; (c) 45 ℃.
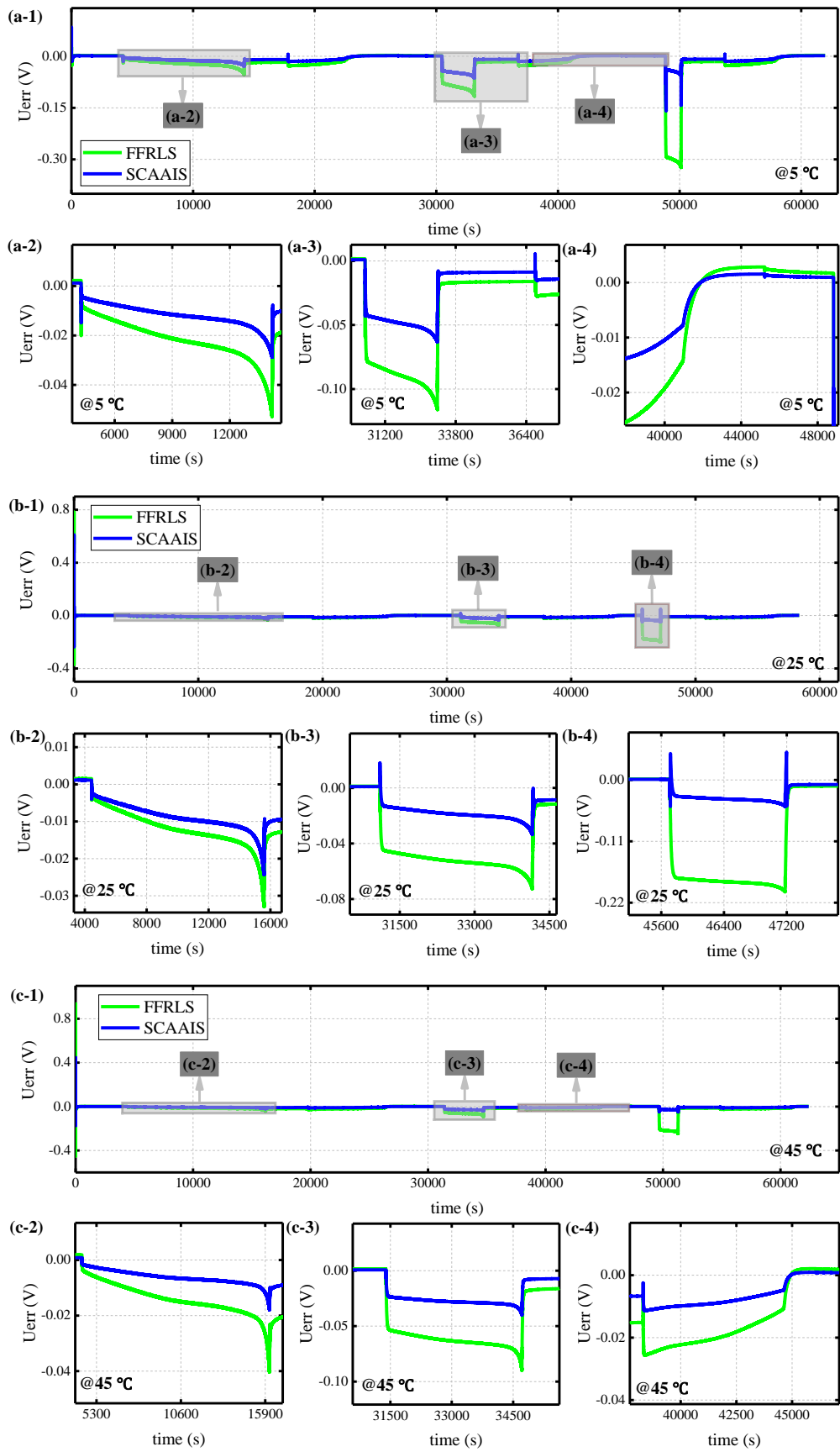
Fig. 17. Terminal voltage prediction error under FCFDT: (a) 5 ℃; (b) 25 ℃; (c) 45 ℃.

In Fig. 16 and Fig. 17, similar to the internal temperature estimation results, the predicted results of

terminal voltage fluctuate within a certain range when the battery is excited by current pulses. By observing the HPPCC experimental results shown in Fig. 16, it can be found that the maximum value of the battery terminal voltage prediction error under the FFRLS method is 36.2 mV, while the maximum value of the battery terminal voltage prediction error under SCAAIS is 17.8 mV. From the FCFDT experimental results shown in Fig. 17, it can be found that the terminal voltage error in the constant current charging and discharging stage based on SCAAIS can be increased by a maximum of 25.8 mV. It is worth noting that both conditions show large errors at the end of battery discharge. One of the main reasons is that with the progress of the experiment, the internal resistance of the battery increases, and the OCV acquisition will inevitably have errors, and the voltage fluctuation will also become severe. In addition, combined with Fig. 16 and Fig.17, it can be seen that the terminal voltage error fluctuation under the HPPCC experimental is larger than that under the FCFDT. One of the main reasons is that the complexity and duration of the HPPCC experimental are higher than those of the FCFDT. Further, the index RMSE and MAE are used to quantitatively calculate the accuracy of the model under different working conditions at each temperature, and the calculation results are shown in **Table 2**.

Table 2 RMSE and MAE of the terminal voltage prediction error under different operating conditions

	HPPCC					
	5 ℃		25 ℃		45 ℃	
	FFRLS	SCAAIS	FFRLS	SCAAIS	FFRLS	SCAAIS
RMSE (V)	0.0193	0.0119	0.0207	0.0109	0.0197	0.0119
MAE (V)	0.0101	0.0061	0.0106	0.0056	0.0106	0.0064
	FCFDT					
	5 ℃		25 ℃		45 ℃	
	FFRLS	SCAAIS	FFRLS	SCAAIS	FFRLS	SCAAIS
RMSE (V)	0.0627	0.0180	0.0336	0.0117	0.0529	0.0118
MAE (V)	0.0293	0.0120	0.0183	0.0097	0.0272	0.0087

Observing the quantitative calculation results shown in **Table 2**, it can be found that the terminal voltage error RMSE and MAE based on the SCAAIS method are lower than those of the traditional FFRLS algorithm under different working conditions. Among them, the RMSE of the terminal voltage

prediction error under the HPPCC experiment decreased by 7.4 mV, 9.8 mV, 7.8 mV, and the MAE decreased by 4.0 mV, 5.0 mV, 4.2 mV at 5 ℃, 25 ℃ and 45 ℃, respectively. The RMSE of the terminal voltage prediction error under the FCFDT experiment decreased by 44.7 mV, 21.9 mV, 41.1 mV, and the MAE decreased by 17.3 mV, 8.6 mV, 18.5 mV at 5 ℃, 25 ℃ and 45 ℃, respectively. Two main reasons lead to this result: firstly, it is the accurate internal temperature result that enables the SCAAIS method to have optimal parameter configuration values in the iterative process; secondly, the multi-time scale effect of the electric characteristic parameters is considered, so that the electrochemical polarization and concentration polarization process information of the carrier in the battery are separated in different frequency bands, and the mixed influence between different characteristic parameters is reduced.

4.4 Evaluation and analysis of parameters dispersion

As shown by the experimental results above, the lumped thermoelectric coupling model established in this paper has excellent internal temperature estimation accuracy and good terminal voltage prediction ability under the iteration of SCAAIS. For battery modeling, the prediction accuracy requirement of terminal voltage can be achieved in most of the existing studies, just like the prediction results of traditional FFRLS algorithm. However, we believe that a high-accuracy battery model should also take into account the changes in internal parameters, which are especially obvious under the electrical characteristics parameters. An example is that even at the same temperature, the same internal electrical characteristic parameters identified by different test current distributions show great differences. Therefore, in addition to evaluating the prediction accuracy of the external characteristics of the battery, the consistency verification of the internal parameter identification results is also important in the analysis. For the electrical characteristics sub-model, we select the identification results of parameters

in the experimental convergence period (HPPPC takes 15000 s, FCFDT takes 3000 s), as shown in **Table 3**. By comparing the time constants obtained by different algorithms under different environments and working conditions, the effectiveness, reliability and superiority of the proposed algorithm are further discussed.

Table 3 Parameter convergence value and time constant calculation with different methods under different conditions

	HPPCC					
	5 ℃		25 ℃		45 ℃	
	FFRLS	SCAAIS	FFRLS	SCAAIS	FFRLS	SCAAIS
R_{ohm} (mΩ)	1.020	1.200	0.980	0.464	0.760	0.266
R_{ct} (mΩ)	0.035	0.664	0.018	0.281	0.014	0.187
C_{dl} (kF)	6.546	13.726	8.753	20.353	9.392	22.548
R_{df} (mΩ)	0.966	2.670	0.585	1.220	0.347	0.801
C_{df} (kF)	47.883	222.524	62.481	262.697	71.469	314.665
τ_{cd} (s)	**0.229**	**9.114**	**0.157**	**5.719**	**0.131**	**4.216**
τ_{df} (s)	**46.255**	**594.139**	**36.551**	**320.490**	**24.800**	**252.047**
	FCFDT					
	5 ℃		25 ℃		45 ℃	
	FFRLS	SCAAIS	FFRLS	SCAAIS	FFRLS	SCAAIS
R_{ohm} (mΩ)	1.053	1.218	0.991	0.475	0.833	0.268
R_{ct} (mΩ)	0.026	0.725	0.012	0.322	0.006	0.184
C_{dl} (kF)	10.771	13.479	12.631	19.030	15.637	24.262
R_{df} (mΩ)	0.753	2.574	0.503	1.124	0.316	0.778
C_{df} (kF)	62.128	237.433	78.038	275.044	86.694	324.420
τ_{cd} (s)	**0.280**	**9.772**	**0.152**	**6.128**	**0.094**	**4.464**
τ_{df} (s)	**46.782**	**611.153**	**39.253**	**309.150**	**27.395**	**252.399**

In **Table 3**, τ_{cd} is the time constant under fast dynamics, corresponding to the charge transfer and electric double-layer process of the battery; τ_{df} is the time constant under slow dynamics, corresponding to the diffusion process of lithium ions in solid particles. By observing **Table 3**, an important information can be found that the time constant obtained by the traditional single-time scale FFRLS method is much smaller than the proposed multi-time scale SCAAIS, especially the time constant τ_{df} value under the diffusion process. The main reason for this result is that the single-time scale FFRLS method cannot obtain enough valuable information in the iterative process due to data saturation. In addition, the electrochemical polarization of the carriers is confused with the concentration

polarization process under long-term cycling conditions. The method proposed in this paper distinguishes and characterizes electrochemical polarization and concentration polarization processes through the idea of multi-feature separation modeling, and realizes asynchronous identification of charge transfer impedance under fast dynamics and diffusion impedance under slow dynamics. This result verifies the effectiveness of the proposed SCAAIS method and proves the reliability of the parameter identification results based on the SCAAIS method.

In addition, another important information can be found in the time constant calculation results at different temperatures, that is, there is a strong correlation between the temperature and the time constant of the impedance link. The conclusion here is that the higher the temperature, the smaller the time constants of the different impedance links. One of the main reasons for this result is that the chemical reaction rate of the battery internal polarization process faster at high temperature than at low temperature. In order to more intuitively demonstrate the superiority of the model combined with the proposed method, we give the concept of the dispersion degree of model parameters to describe the rationality and effectiveness of different identification methods. In order to more intuitively demonstrate the superiority of the model combined with the proposed method, we give a new concept of dispersion based on the consistency of the model parameters to describe the rationality and effectiveness of different identification methods. The specific implementation is as follows: firstly, normalize the parameter identification results under different methods; then calculate the difference of the normalized results; and finally use the percentage of the difference to define the dispersion of parameters under different identification methods. The normalized values and parameter dispersion results of different methods under different working conditions at different temperatures are shown in Fig. 18.
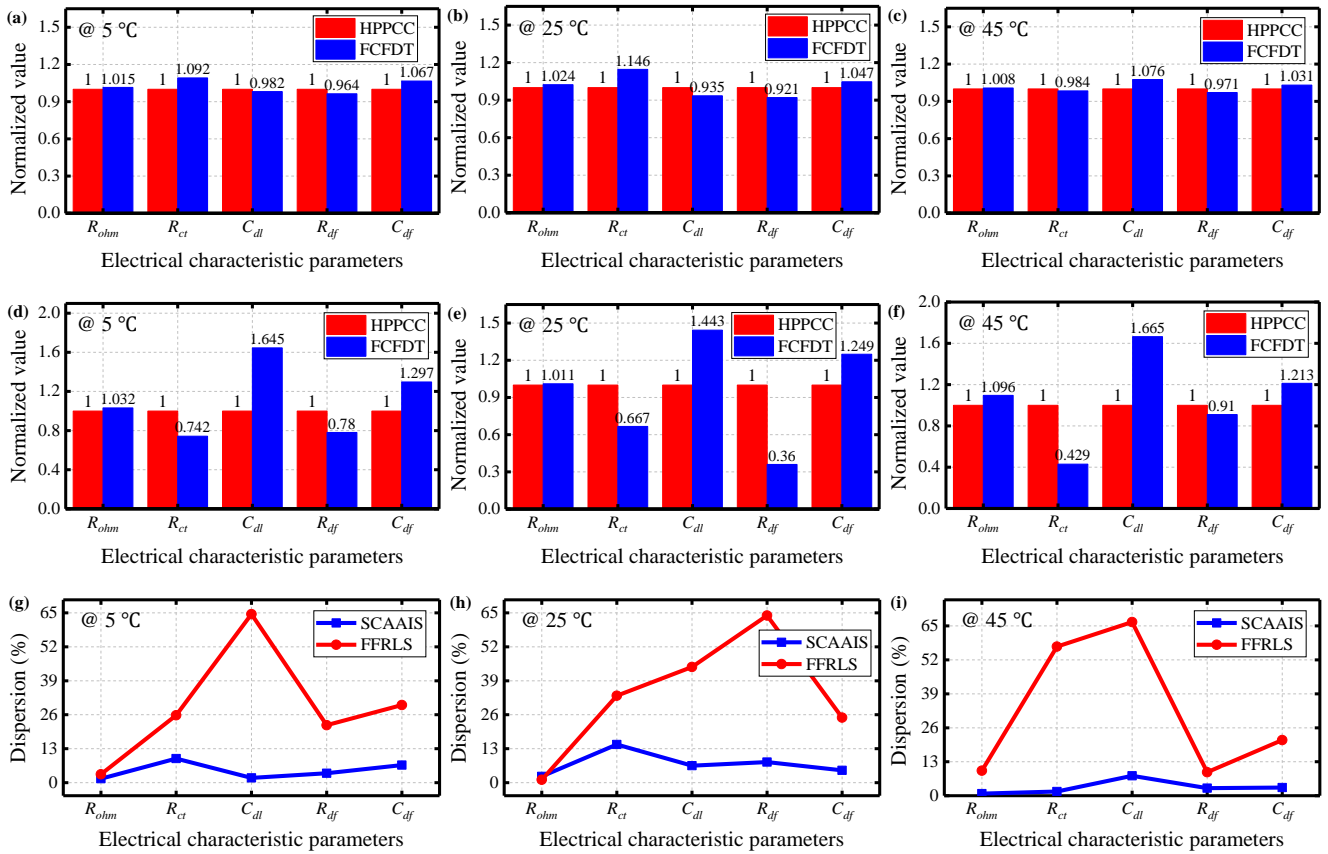
Fig. 18. Consistency results of electrical characteristic parameters under different identification methods: (a) SCAIS at 5 ℃; (b) SCAIS at 25 ℃; (c) SCAIS at 45 ℃; (d) FFRLS at 5 ℃; (e) FFRLS at 25 ℃; (f) FFRLS at 45 ℃; (g) Dispersion at 5 ℃; (h) Dispersion at 25 ℃; (i) Dispersion at 45 ℃.

Fig. 18 shows the parameter identification results under different methods are uniformly normalized to the parameter values obtained under the HPPCC condition. Observing Fig. 18, it can be seen that the parameter identification results of the proposed SCAAIS at different temperatures all show better consistency, and the dispersion of parameters is significantly reduced compared with the traditional single-time scale FFRLS. Among them, the dispersion calculation results shown in Fig. 18(g) to Fig. 18(i) show that the maximum dispersion of the parameters identified based on the SCAAIS method is 14.6%; and the maximum dispersion of the parameters identified based on the traditional single-time scale FFRLS method is 66.5%. This further reflects the superiority of the proposed SCAAIS method combining the precise internal temperature correction mechanism and the idea of multi-feature separation modeling. In addition, it can also be found from the calculation results of parameter

consistency that the ohmic internal resistance identified by the two methods shows good consistency under different working conditions at different temperatures. A major reason is that the identification of the ohmic internal resistance is not affected by the accumulation time of the current excitation.

5 Conclusions

In this paper, the influence of multi-time scale effects and external heat transfer efficiency on the thermoelectric coupling modeling of batteries are studied. A strong coupling adaptive asynchronous identification strategy is designed by proposing multi-feature separation modeling idea. Compared with the traditional single-time scale forgetting factor recursive least squares method, the five main conclusions of this study are as follows.

(1). The complex thermoelectric coupling modeling of batteries can be described by the equivalent circuit model. In the traditional single-time scale identification method, relevant valuable information will be lost due to data saturation during iteration, and the two polarization reaction processes will be confused, resulting in inaccurate parameter identification results.

(2). For the commercial $LiFePO_4$ 18650 battery cells in this paper, the high-frequency kinetic response is completed within ten seconds, and the low-frequency kinetic response is completed within several hundred seconds. Under this dynamic performance, a multi-feature separation modeling idea is proposed, in which the fast dynamics parameters and the slow dynamics parameters are identified on different time scales.

(3). Since the different use environments of the battery will lead to different external heat transfer efficiencies, the robustness of the external thermal resistance in the lumped thermoelectric coupling model is discussed by setting different initial values. The results show that under different initial value settings, the external thermal resistance can quickly converge to the accurate value.

(4). The verification results of two complex cycle tests show that, compared with the traditional single-time scale method without considering the uncertainty of external thermal resistance, the maximum RMSE of the terminal voltage tracking error of the proposed method under the two operating conditions at different temperatures is reduced by 9.8 mV and 44.7 mV, respectively, the maximum MAE decreased by 5.0 mV and 18.5 mV, respectively; the maximum RMSE of the internal temperature estimation error decreases by 1.101 ℃ and 1.119 ℃, and the maximum MAE decreases by 1.104 ℃ and 1.128 ℃, respectively.

(5). The discreteness concept of parameter identification is proposed and discussed in this paper. The experimental results show that the maximum dispersion of the electrical characteristic parameter identification results of the proposed method and the traditional single-time scale method are 14.6 and 66.5%, respectively, and the proposed method improves the parameter consistency by 51.9%.

Acknowledgments

References

[1] Wang, YJ; Zhang, XC; Chen, ZH. Low temperature preheating techniques for Lithium-ion batteries: Recent advances and future challenges. *Applied Energy* **2022**; 313: 118832.

[2] Zhang, ZQ; Huang, GX; Tang, XL; Yin, HR; Kang, JC; Zhang, QH; et al. Zn and Na promoted Fe catalysts for sustainable production of high-valued olefins by CO2 hydrogenation. *Fuel* **2022**; 309: 122105.

[3] Jiang, SD; Song, ZX. A review on the state of health estimation methods of lead-acid batteries. *Journal of Power Sources* **2022**; 517: 230710.

[4] Tang, XP; Wang, YJ; Zou, CF; Yao, K; Xia, YX; Gao, FR. A novel framework for Lithium-ion battery modeling considering uncertainties of temperature and aging. *Energy Conversion and Management* **2019**; 180: 162-170.

[5] Severson, KA; Attia, PM, Jin, N; Perkins, N; Jiang, B; Yang, Z; et al. Data-driven prediction of battery cycle life before capacity degradation. *Nature Energy* **2019**; 4: 383-391.

[6] Su, BZ; Wu, SL; Liang, HQ; Gu, QF; Wang, HM; Zhou, WC; et al. Boosting capacity and operating voltage of LiVO3 as cathode for lithium-ion batteries by activating oxygen reaction in the lattice. *Journal of Power Sources* **2022**; 517: 230728.

[7] Duffner, F; Kronemeyer, N; Tubke, J; Leker, J; Winter, M; Schmuch, R. Post-lithium-ion battery cell production and its compatibility with lithium-ion cell production infrastructure. *Nature Energy* **2021**; 6: 123-134.

[8] Chen, X; Zhou, F; Yang, W; Gui, Y; Zhang, Y. A hybrid thermal management system with liquid cooling and composite phase change materials containing various expanded graphite contents for cylindrical lithium-ion batteries. *Applied Thermal Engineering* **2022**; 200: 117702.

[9] Wang, YJ; Tian, JQ; Sun, ZD; Wang, L; Xu, RL; Li, MC; et al. A comprehensive review of battery modeling and state estimation approaches for advanced battery management systems. *Renewable & Sustainable Energy Reviews* **2020**; 131: 110015.

[10] Wang, YJ; Xu, RL; Zhou, CJ; Kang, X; Chen, ZH. Digital twin and cloud-side-end collaboration for intelligent battery management system. *Journal of Manufacturing Systems* **2022**; 62: 124-134.

[11] Zhu, C; Shang, YL; Lu F, Jian, Y; Cheng, CW; Mi, C. Core temperature estimation for self-heating automotive lithium-ion batteries in cold climates. *IEEE Transactions on Industrial Informatics* **2022**; 16: 3366–3375.

[12] Xie, Y; Li, W; Hu, XS; Lin, XK; Zhang, YJ; Dan, D; et al. An enhanced online temperature estimation for lithium-ion batteries. *IEEE Transactions on Transportation Electrification* **2020**; 6(2): 375–390.

[13] Xu, CS; Zhang, FS; Feng, XN; Jiang, FC; Ren, DS; Lu, LG; et al. Experimental study on thermal runaway propagation of lithium-ion battery modules with different parallel-series hybrid connections. *Journal of Cleaner Production* **2021**; 284: 124749.

[14] Hu, Y; Wang, YY. Two time-scaled battery model identification with application to battery state estimation. *IEEE Transactions on Control Systems Technology* **2015**; 23: 1180–8.

[15] Wang, YJ; Chen, ZH. A framework for state-of-charge and remaining discharge time prediction using unscented particle filter. *Applied Energy* **2020**; 260: 114324.

[16] Liu, SZ; Chen, JJ; Zhang, C; Jin, L; Yang, QX. Experimental study on lithium-ion cell characteristics at different discharge rates. *Journal of Energy Storage* **2022**; 45: 103418.

[17] Andriunas, I; Milojevic, Z; Wade, N; Das, PK. Impact of solid-electrolyte interphase layer thickness. *Journal of Energy Storage* **2022**; 525: 231126.

[18] Li, DZ; Wang, LC; Duan, CX; Li, Q; Wang, K. Temperature prediction of lithium-ion batteries based on electrochemical impedance spectrum: A review. *International Journal of Energy Research* **2022**; DOI: 10.1002/er.7905.

[19] Pals, CR. Thermal modeling of the lithium/polymer battery. *Journal of the Electrochemical Society* **1994**; 142(10): 3274-3281.

[20] Kim, Y; Mohan, S; Siegel, JB; Stefanopoulou, AG; Ding, Y. The estimation of radial temperature distribution in cylindrical battery cells under unknown cooling conditions. *IEEE Conference on Decision and Control* **2013**; 5680-5685.

[21] Torchio, M; Magni, L; Gopaluni, RB; Braatz, RD; Raimondo, DM. LIONSIMBA: A Matlab framework based on a finite volume model suitable for Li-ion battery design, simulation and control. *Journal of the Electrochemical Society* **2016**; 163(7): A1192-A1205.

[22] Mei, WX; Chen, HD; Sun, JH; Wang, QS. Numerical study on tab dimension optimization of lithium-ion battery from the thermal safety perspective. *Applied Thermal Engineering* **2018**; 142: 148-165.

[23] Ding, QY; Wang, YJ; Chen, ZH. Parameter identification of reduced-order electrochemical model simplified by spectral methods and state estimation based on square-root cubature Kalman filter. *Journal of Energy Storage* 2022; 46: 103828.

[24] Wu, LX; Liu, K; Pang, H. Evaluation and observability analysis of an improved re duce d-order electrochemical model for lithium-ion battery. *Electrochemica Acta* **2021**; *368*: 137604.

[25] Tian, JQ; Wang, YJ; Chen, ZH. An improved single particle model for lithium-ion batteries based on main stress factor compensation. *Journal of Cleaner Production* **2021**; 278: 123456.

[26] Wu, LX; Pang H; Geng, YF; Liu, JH; Liu K. Low-complexity state of charge and anode potential prediction for lithium-ion batteries using a simplified electrochemical model-based observer under variable load condition. *International Journal of Energy Research* **2022**; 1-15.

[27] Xu, M; Zhang, ZQ; Wang, X; Jia, L; Yang, LX. Two-dimensional electrochemical thermal coupled modeling of cylindrical LiFePO4 batteries. *Journal of Power Source* **2014**; 256: 233-243.

[28] Wu, LX; Liu, K; Pang, H. Online SOC estimation based on simplified electrochemical model for lithium-ion batteries considering current bias. *Energies* **2021**; 14: 5265.

[29] Li, WH; Fan, Y; Ringbeck, F; Jost, D; Sauer, DU. Unlocking electrochemical model-based online power prediction for lithium-ion batteries via Gaussian process regression. *Applied Energy* **2022**; 306: 118114.

[30] Barillas, JK; Li, JH; Gunther, C; Danzer, MA. A comparative study and validation of state estimation algorithms for Li-ion battery management systems. *Applied Energy* **2015**; 155: 455-62.

[31] Raijmakers, LHJ; Danilov, DL; Eichel, RA; Notten, PHL. A review on various temperature-indication methods for Li-ion batteries. *Applied Energy* **2019**; *240*: 918-945.

[32] Wang, YJ; Zhou, CJ; Chen, ZH. Optimization of battery charging strategy based on nonlinear model predictive control. *Energy* **2022**; 241: 122877.

[33]Wang, YJ; Zhou, CJ; Zhao, GH; Chen, ZH. A framework for battery internal temperature and state-of-charge estimation based on fractional-order thermoelectric model. *Transactions of The Institute of Measurement and Control* **2022**; 01423312211067293.

[34] Chen, ZY; Zhang, B; Xiong, R; Shen, WX; Yu, QQ. Electro-thermal coupling model of lithium-ion batteries under external short circuit. *Applied Energy* **2021**; 293: 116910.

[35] Chen, J; Ren, DS; Hsu, HJ; Wang, L; He, XM; Zhang, CP; et al. MG. Investigating the thermal runaway features of lithium-ion batteries using a thermal resistance network model. *Applied Energy* **2021**; 295: 117038.

[36] Shi, HT; Wang, SL; Wang, LP; Xu, WH; Carlos, F; Dablu, BE; et al. On-line adaptive asynchronous parameter identification of lumped electrical characteristic model for vehicle lithium-ion battery considering multi-time scale effects. *Journal of Power Sources* **2022**; 515: 230725.

[37] Gabano, JD; Poinot, T; Huard, B. Bounded diffusion impedance characterization of battery electrodes using fractional modeling. *Communications in Nonlinear Science and Numerical Simulation* **2017**; 47: 164-177.

[38]Song, JH; Bazant, MZ. Effects of Nanoparticle Geometry and Size Distribution on Diffusion Impedance of Battery Electrodes. *Journal of the Electrochemical Society* **2013**; 106: 15-24.

[39] Tang, XP; Wang, YJ; Zou, CF; Yao, K; Xia, YX; Gao, FR. A novel framework for Lithium-ion battery modeling considering uncertainties of temperature and aging. *Energy Conversion and Management* **2019**; 180: 162-170.

[40] Zhang, X; Wang, YJ; Wu, J; Chen, ZH. A novel method for lithium-ion battery state of energy and state of power estimation based on multi-time-scale filter. *Applied Energy* **2018**; 216: 442-451.

[41] Shi, HT; Wang, SL; Carlos, F; Yu, CM; Fan, YC; Cao W. Improved splice-electrochemical circuit polarization modeling and optimized dynamic functional multi-innovation least square parameter identification for lithium-ion batteries. *International Journal of Energy Research* **2021**; 45: 15323.

[42] Xu, J; Mei, XS; Wang, X; Fu, YM; Zhao, YF; Wang, JP. A relative state of health estimation method based on wavelet analysis for lithium-ion battery cells. *IEEE Transactions on Industrial Electronics* **2021**; 68: 6973-6981.

[43] Deng, ZW; Lin, XK; Cai, JW; Hu, XS. Battery health estimation with degradation pattern recognition and transfer learning. *Journal of Power Sources* **2022**; 525: 231027.

[44] Hu Y, Wang YY. Real time battery model identification using a two time-scaled approach. *In: Proceedings of ASME dynamic system control conference* **2013**; V003T41A002-1-V003T41A007.

[45] Dai, HF; Xu, TJ; Zhu, LT. Adaptive model parameter identification for large capacity Li-ion batteries on separated time scales. *Applied Energy* **2016**; 181: 119-131.

[46] Tang, XP; Wang YJ; Yao K; He ZW; Gao, FR. Model migration based battery power capability evaluation considering uncertainties of temperature and aging. *Journal of Power Sources* **2019**; 440: 227141.

[47] He, HW; Zhang, XW; Xiong, R; Xu, YL; Guo, HQ. Online model-based estimation of state-of-charge and open-circuit voltage of lithium-ion batteries in electric vehicles. *Energy* **2012**; 39: 310-318.

[48] Wang, YJ; Chen, ZH. A framework for state-of-charge and remaining discharge time prediction using unscented particle filter. *Applied Energy* **2020**; 260,114324.

[49] Song, YC; Peng, Y; Liu, DT.Model-Based Health Diagnosis for Lithium-Ion Battery Pack in Space Applications. *IEEE Transactions on Industrial Electronics* **2021**; 68(12): 12375-12384.

[50] Shi, HT; Wang, LP; Wang, SL; Carlos, F; Xiong, X; Etse, DB; et al. A novel lumped thermal characteristic modeling strategy for the online adaptive temperature and parameter co-estimation of vehicle lithium-ion batteries. *Journal of Energy Storage* **2022**; 50: 104309.

[51] Ouyang, Q; Chen, J; Zheng, J. State-of-Charge observer design for batteries with online model parameter identification: a robust approach. *IEEE Transactions on Power Electronics* **2020**; 35(6): 5820-5831.

[52] Jiang, C; Wang, SL; Wu, B; Carlos, F; Xiong, X; James, CK. A state-of-charge estimation method of the power lithium-ion battery in complex conditions based on adaptive square root extended Kalman filter. *Energy* **2021**; 219: 119603.

[53] Pan, HH; Lu, ZQ; Lin, WL; Li, JZ; Chen, L. State of charge estimation of lithium-ion batteries using a grey extended Kalman filter and a novel open-circuit voltage model. *Energy* **2017**; 138: 764-775.

[54] He, HW; Xiong, R; Guo, HQ .Online estimation of model parameters and state-of-charge of LiFePO4 batteries in electric vehicles. *Applied Energy* **2012**; 89: 413-420

[55] Xie, YX; Wang, SL; Fernandez, C; Yu, CM; Cao, W; Chen, XP. Improved gray wolf particle filtering and high-fidelity second-order autoregressive equivalent modeling for intelligent state of charge prediction of lithium-ion batteries. International Journal of Energy Research, **2021**; 45(13): 19203-19214.

Credit Author Statement

Haotian Shi: Conceptualization, Methodology, Validation, Data curation, Writing - Original Draft.

Shunli Wang: Data curation, Methodology, Funding acquisition. **Carlos Fernandez**: Formal analysis, Writing - Review & Editing. **Chunmei Yu**: Writing - Review & Editing, Software.

Wenhua Xu: Writing - Original Draft, Software, Resources. **Bobobee Etse Dablu**: Software, Writing - Original Draft. **Liping Wang**: Writing - Review & Editing, Supervision.